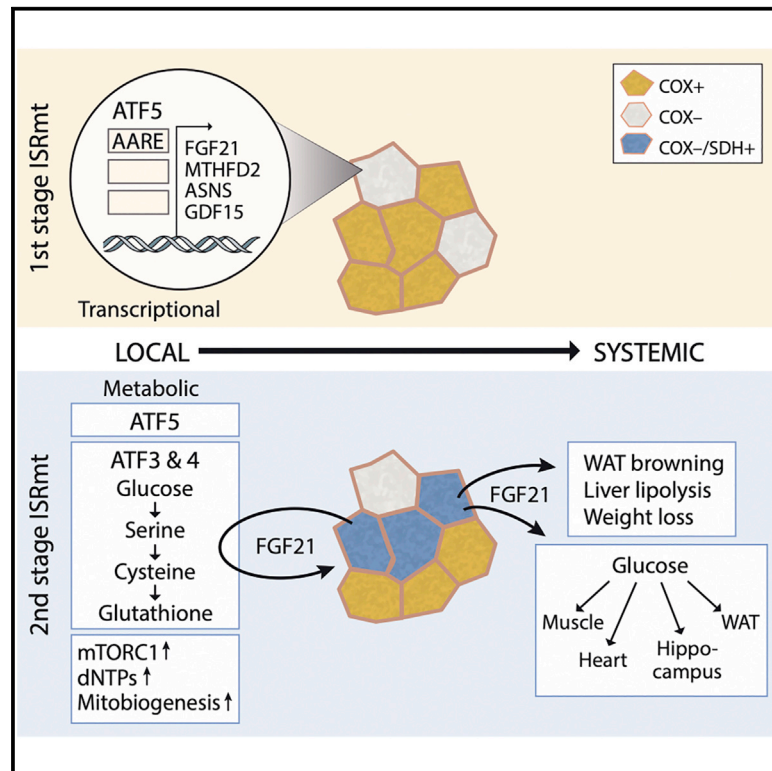# Fibroblast Growth Factor 21 Drives Dynamics of Local and Systemic Stress Responses in Mitochondrial Myopathy with mtDNA Deletions

Graphical Abstract

Authors

Saara Forsström,
Christopher B. Jackson,
Christopher J. Carroll, ...,
Joni Nikkanen, Liliya Euro,
Anu Suomalainen

Correspondence

anu.wartiovaara@helsinki.fi

In Brief

Forsström, Jackson et al. report mechanisms of orchestrated, stage-wise progression of mammalian integrated mitochondrial stress response (ISR^mt) in mitochondrial muscle disease. They identify acute and chronic ISR^mt, with crucial dependence on auto- and endocrine actions of FGF21 hormone, driving local serine biosynthesis, transsulfuration, and signaling from muscle to brain.

Highlights

- Mitochondrial integrated stress response (ISR^mt) progresses in temporal stages

- ISR^mt is conserved in human and mouse diseases with mtDNA stress

- Autocrine FGF21 drives serine synthesis and transsulfuration in muscle

- Endocrine FGF21 drives disease-related glucose uptake in dorsal hippocampus

Cell Metabolism

Article

CellPress

Fibroblast Growth Factor 21 Drives Dynamics of Local and Systemic Stress Responses in Mitochondrial Myopathy with mtDNA Deletions

Saara Forsström,[1,11] Christopher B. Jackson,[1,11] Christopher J. Carroll,[1,2] Mervi Kuronen,[1] Eija Pirinen,[3]
Swagat Pradhan,[1] Anastasiia Marmyleva,[1] Mari Auranen,[4] Iida-Marja Kleine,[1] Nahid A. Khan,[1] Anne Roivainen,[5,6]
Päivi Marjamäki,[5] Heidi Liljenbäck,[5,6] Liya Wang,[7] Brendan J. Battersby,[8] Uwe Richter,[8] Vidya Velagapudi,[9]
Joni Nikkanen,[1] Liliya Euro,[1] and Anu Suomalainen[1,4,10,12,*]

[1]Stem Cells and Metabolism Research Program, Faculty of Medicine, University of Helsinki, 00290 Helsinki, Finland
[2]Molecular and Clinical Sciences Research Institute, St. George's University of London, London SW170RE, UK
[3]Clinical and Molecular Metabolism Research Program, Faculty of Medicine, University of Helsinki, 00290 Helsinki, Finland
[4]Department of Neurosciences, Helsinki University Central Hospital, 00290 Helsinki, Finland
[5]Turku PET Centre, University of Turku, 20520 Turku, Finland
[6]Turku Center for Disease Modeling, Institute of Biomedicine, University of Turku, 20520 Turku, Finland
[7]Department of Anatomy, Physiology, and Biochemistry, Swedish University of Agricultural Sciences, 75007 Uppsala, Sweden
[8]Institute of Biotechnology, University of Helsinki, 00790 Helsinki, Finland
[9]Metabolomics Unit, Institute for Molecular Medicine Finland FIMM, HiLIFE, University of Helsinki, 00290 Helsinki, Finland
[10]Neuroscience Center, University of Helsinki, 00290 Helsinki, Finland
[11]These authors contributed equally
[12]Lead Contact
*Correspondence: anu.wartiovaara@helsinki.fi
https://doi.org/10.1016/j.cmet.2019.08.019

SUMMARY

Mitochondrial dysfunction elicits stress responses that safeguard cellular homeostasis against metabolic insults. Mitochondrial integrated stress response (ISR[mt]) is a major response to mitochondrial (mt)DNA expression stress (mtDNA maintenance, translation defects), but the knowledge of dynamics or interdependence of components is lacking. We report that in mitochondrial myopathy, ISR[mt] progresses in temporal stages and development from early to chronic and is regulated by autocrine and endocrine effects of FGF21, a metabolic hormone with pleiotropic effects. Initial disease signs induce transcriptional ISR[mt] (ATF5, mitochondrial one-carbon cycle, FGF21, and GDF15). The local progression to 2nd metabolic ISR[mt] stage (ATF3, ATF4, glucose uptake, serine biosynthesis, and transsulfuration) is FGF21 dependent. Mitochondrial unfolded protein response marks the 3rd ISR[mt] stage

of failing tissue. Systemically, FGF21 drives weight loss and glucose preference, and modifies metabolism and respiratory chain deficiency in a specific hippocampal brain region. Our evidence indicates that FGF21 is a local and systemic messenger of mtDNA stress in mice and humans with mitochondrial disease.

INTRODUCTION

Mitochondrial diseases show an unprecedented clinical variability, but the molecular mechanisms underlying their tissue-specific manifestations are poorly understood (Gorman et al., 2016; Nunnari and Suomalainen, 2012). Recent evidence suggests that metabolic responses elicited by different mitochondrial insults are specific for tissue type and dysfunction (Suomalainen and Battersby, 2018), raising an exciting question of whether the responses contribute to tissue-specific manifestations of the disease.

Context and Significance

Mitochondrial disorders happen when the cell's powerplants (mitochondria) fail to produce enough energy for the body to function properly and exhibit a diverse array of clinical manifestations. Progressive muscle weakness and dysfunction in the respiration apparatus underlie mitochondrial myopathy (MM). The group of Anu Suomalainen from Helsinki University shows that the metabolic regulator Fibroblast growth factor 21 (FGF21) coordinates step-wise changes within the muscle cell and in other tissues of the body in the mouse and in humans to progress MM, including changes in glucose and lipid metabolism, weight loss, and brain defects. The work highlights how a muscle disease can affect brain metabolism and emphasizes the importance of considering the whole body holistically when assessing diseases and treatments.

The first mitochondrial stress response, mitochondrial unfolded protein response (UPR^{mt}), was characterized in mammalian cultured cells and in the worm *C. elegans* (Durieux et al., 2011; Haynes et al., 2007, 2013; Merkwirth et al., 2016). Proteotoxic stress activates UPR^{mt} through ATFS-1 (stress-activated transcription factor S1) that relocates from mitochondria to nucleus, binds to promoters with amino acid response elements (AAREs), and induces transcription of mitochondrial heat shock proteins (HSPs), chaperones, and proteases (Haynes et al., 2013; Nargund et al., 2012). In the worm, neuronal inactivation of mitochondrial cytochrome *c* oxidase elicited UPR^{mt} locally, but also in the gut, pointing to a secreted factor mediating stress signals from the affected neurons to periphery (Durieux et al., 2011). The worm "mitokine" was recently reported to be a Wnt-ligand/EGL-20 (Zhang et al., 2018). However, in mice with mitochondrial dysfunction, UPR^{mt}/HSP induction has been mild if present (Pulliam et al., 2014; Seiferling et al., 2016), leaving the role of UPR^{mt} in primary mitochondrial diseases open.

MM manifests as progressive muscle weakness and respiratory chain (RC) dysfunction, typically caused by mtDNA deletions or mtDNA expression defects (mtDNA maintenance, translation; MM denoting diseases associated with these defects from now on). MM mice present a robust transcriptional stress response with induction of AARE-regulated genes and major remodeling of whole-cellular anabolic pathways, including serine, glutathione, and purine biosynthesis (Bao et al., 2016; Kühl et al., 2017; Nikkanen et al., 2016). This mitochondrial integrated stress response (ISR^{mt}), with metabolic and transcriptional components, is regulated by mTORC1 (mechanistic target of rapamycin C1), a major signal and growth integrator kinase (Khan et al., 2017; Zhang et al., 2013). In mammals, ISR^{mt} is a robust response to mtDNA stress, integrating mitochondrial and cytoplasmic metabolism to pathways of growth and repair.

One of the most upregulated ISR^{mt} components in humans and mice with MM is fibroblast growth factor 21 (FGF21). FGF21 has manifold roles in regulation of lipid and glucose metabolism, getting activated by low blood lipids and glucose; inducing ketone body synthesis, lipolysis, and browning in white adipose tissue (WAT); improving glucose tolerance; and regulating food intake (Badman et al., 2007; Inagaki et al., 2007; Kharitonenkov and Shanafelt, 2009; Kharitonenkov et al., 2005; Potthoff, 2017). So far, however, MM diseases are the only group of inherited diseases that consistently induces FGF21 in a genotype- and phenotype-specific manner. In mice and humans with MM, FGF21 is chronically secreted from the affected muscle fibers and/or heart independent of the feeding state (Agnew et al., 2018; Dogan et al., 2014; Keipert et al., 2014; Lehtonen et al., 2016; Ost et al., 2016; Pereira et al., 2017; Suomalainen et al., 2011; Tyynismaa et al., 2010). Interestingly, however, the response is specific to mtDNA expression diseases, whereas structural defects of the RC enzymes do not elicit a similar response (Lehtonen et al., 2016). These data indicate that different types of mitochondrial dysfunction induce different stress responses.

Here, we report that mammalian ISR^{mt} progresses in temporal stages, and its components vary in different tissue types and disease stages, in post-mitotic or proliferating cell types. We show that FGF21 orc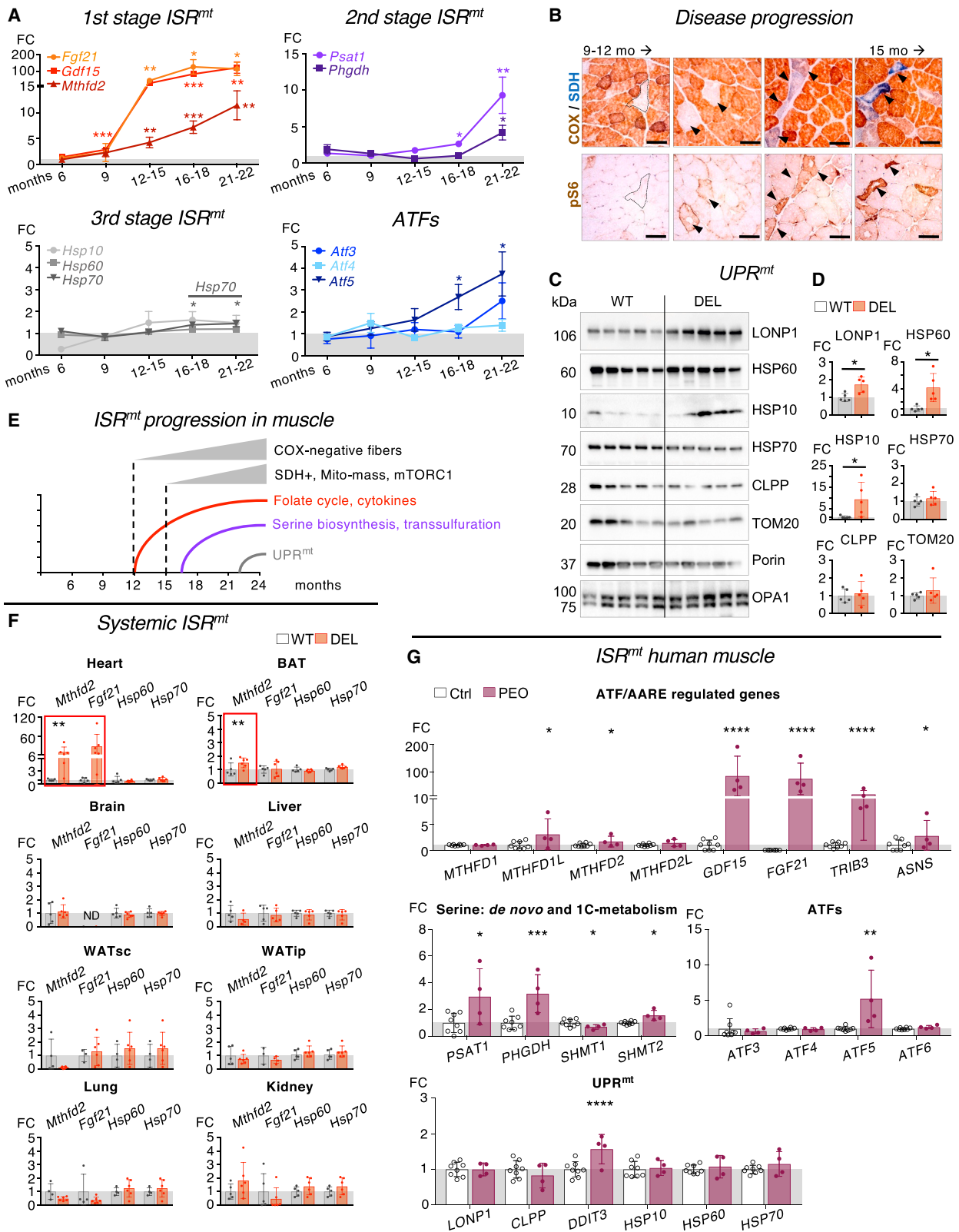hestrates progression of ISR^{mt} and MM into systemic disease, with major effects for glucose and lipid metabolism, weight loss, and brain manifestation of MM. Our data indicate that mitochondrial stress responses are (1) only partially conserved in species and (2) not generalizable between organisms or even mammalian cell types, and (3) that FGF21 is a key mediator of metabolic remodeling and progression of ISR^{mt} locally and systemically.

RESULTS

ISR^{mt} Progresses in Temporal Stages, Involves Different Activating Transcription Factors (ATFs) at Different Disease Stages, and Is Partly Distinct from UPR^{mt} and UPR^{Er}

The various arms of ISR^{mt} (UPR^{mt}, ATF/AARE, endocrine factors, and metabolic remodeling) prompted us to ask whether the different components are induced in all-or-none, parallel, or sequential manner in MM mice, *in vivo*. We utilized the Deletor mice that show robust ISR^{mt} (Khan et al., 2017; Nikkanen et al., 2016; Tyynismaa et al., 2010) despite mild MM findings and normal lifespan (Tyynismaa et al., 2005). The Deletors accumulate mtDNA deletions and show progressive RC deficiency in skeletal muscle and heart, as a consequence of ubiquitous expression of a dominant patient mutation in Twinkle, nuclear-encoded replicative helicase of mtDNA. These mice offer an excellent opportunity to dissect the long-term stress response dynamics upon MM progression. The first ISR^{mt} signs in Deletor muscle coincide with the initial histological signs of RC deficiency (mosaic partial or complete cytochrome *c* oxidase [COX] deficiency) in <12-month-old mice and involve highly activated transcription of *Fgf21* and *Mthfd2* as well as *Gdf15* (Figures 1A and 1B). At 14–16 months, some COX-deficient fibers start to show increased mitochondrial mass and activity of succinate dehydrogenase (SDH, RC complex II, exclusively nuclear-encoded and, therefore, not affected by mtDNA deletions) (Figure 1B). At this time, the second phase of ISR^{mt} involves activation of *Atf5* and the regulatory enzymes of *de novo* serine biosynthesis (phosphoglycerate dehydrogenase [*Phgdh*] and phosphoserine aminotransferase 1 [*Psat1*]) (Figure 1A), as well as mTORC1 (elevated phosphorylation of ribosomal S6 protein) (Figure 1B). These results indicate that ISR^{mt} induction progresses in orderly temporal stages.

We then asked whether UPR^{mt} is part of ISR^{mt} in mammals. In Deletors of >21 months of age, mitochondrial HSP70 transcripts increase slightly, while mitochondrial HSP10 and HSP60 remain unchanged (Figure 1A). In >24-month-old Deletor muscle LonP1 (Lon peptidase 1), HSP60 and HSP10 protein amounts are increased in mitochondrial extracts, while HSP70 and CLPP (caseinolytic mitochondrial matrix peptidase) are wild-type (WT)-like (Figures 1C and 1D). At this late stage, *Atf3* gets induced (Figure 1A). These data suggest that the affected skeletal muscle manifests a sequential ATF response, *Atf5* being progressively induced from the 1st to 2nd ISR^{mt} stage and leading the response, and *Atf3* participating in terminal stage along with UPR^{mt}. Despite non-significant marginal changes in *Atf4* transcripts, we cannot exclude its post-translational induction in the muscle. In conclusion, ISR^{mt} in mammalian muscle proceeds in three stages that follow disease severity with initial activation of MTHFD2, FGF21, and GDF15; secondary induction of mTORC1,

CellPress

A

1st stage ISR^mt — Fgf21, Gdf15, Mthfd2 (FC vs months: 6, 9, 12-15, 16-18, 21-22)

2nd stage ISR^mt — Psat1, Phgdh (FC vs months)

3rd stage ISR^mt — Hsp10, Hsp60, Hsp70 (FC vs months)

ATFs — Atf3, Atf4, Atf5 (FC vs months)

B *Disease progression*

9-12 mo → ... 15 mo →

COX / SDH

pS6

C *UPR^mt*

kDa WT DEL

106 LONP1
60 HSP60
10 HSP10
70 HSP70
28 CLPP
20 TOM20
37 Porin
100/75 OPA1

D WT DEL — LONP1, HSP60, HSP10, HSP70, CLPP, TOM20 (FC)

E *ISR^mt progression in muscle*

COX-negative fibers
SDH+, Mito-mass, mTORC1
Folate cycle, cytokines
Serine biosynthesis, transsulfuration
UPR^mt

months: 6 9 12 15 18 21 24

F *Systemic ISR^mt* — WT DEL

Heart — Mthfd2, Fgf21, Hsp60, Hsp70 (FC)
BAT — Mthfd2, Fgf21, Hsp60, Hsp70 (FC)
Brain — Mthfd2, Fgf21, Hsp60, Hsp70 (FC) ND
Liver — Mthfd2, Fgf21, Hsp60, Hsp70 (FC)
WATsc — Mthfd2, Fgf21, Hsp60, Hsp70 (FC)
WATip — Mthfd2, Fgf21, Hsp60, Hsp70 (FC)
Lung — Mthfd2, Fgf21, Hsp60, Hsp70 (FC)
Kidney — Mthfd2, Fgf21, Hsp60, Hsp70 (FC)

G *ISR^mt human muscle* — Ctrl PEO

ATF/AARE regulated genes — MTHFD1, MTHFD1L, MTHFD2, MTHFD2L, GDF15, FGF21, TRIB3, ASNS (FC)

Serine: de novo and 1C-metabolism — PSAT1, PHGDH, SHMT1, SHMT2 (FC)

ATFs — ATF3, ATF4, ATF5, ATF6 (FC)

UPR^mt — LONP1, CLPP, DDIT3, HSP10, HSP60, HSP70 (FC)

(legend on next page)

CellPress

Table 1. Clinical Characteristics of MM Patients

	Sex	Age at Sampling	Age of Disease Onset	Disease Cause
Patient 1	F	57	33	single mtDNA deletion
Patient 2	M	55	21	multiple mtDNA deletions[a]
Patient 3	F	54	30	multiple mtDNA deletions[a]
Patient 4	F	70	31	single small mtDNA deletion
Controls n = 8	6 F/2 M	48–64	–	–

[a]Twinkle mutation leading to 13-amino acid insertion in linker domain = homologous mutation to that in Deletor mouse.

transsulfuration, and serine biogenesis; followed by terminal-stage mild UPR[mt] (Figure 1E).

Optic atrophy 1 (OPA1)-dependent membrane remodeling is commonly described as part of mitochondrial stress responses in cell culture and mitochondrial protein knockout mice (MacVicar and Langer, 2016; Olichon et al., 2003; Richter et al., 2013, 2015, 2019). In 24-month-old Deletors with advanced MM, the long isoform of OPA1 remains unprocessed (Figure 1C), showing that OPA1 processing is not an integral part of MM-related ISR[mt]. ISR[mt] is also distinct from endoplasmic reticulum (ER) stress (Gardner et al., 2013; Sidrauski and Walter, 1997; Taylor and Dillin, 2013), based on WT-like binding-immunoglobulin protein (BiP), X-box binding protein 1 (XBP1) splicing, and *Atf6* expression in the aged Deletor muscle (Figures S1A–S1C).

We then asked whether ISR[mt] induction in the muscle sends stress signals to non-affected tissues, similar to UPR[mt] in *C. elegans* (Durieux et al., 2011), but found no evidence for such an event. The key ISR[mt] components are upregulated only in the primarily affected tissues with mtDNA deletions (muscle, heart, and BAT; Figures 1A and 1F), but not, for example, in the liver, a key metabolic organ. Therefore, unlike in the worm, ISR[mt] does not spread per se in mammalian tissues via a secreted factor.

ISR[mt] Is Conserved in Human Patients with mtDNA Deletions

FGF21 shows high concentrations in the serum and muscle of MM patients, compared to other mitochondrial or non-mitochondrial muscle diseases (Lehtonen et al., 2016; Suomalainen et al., 2011). To examine which parts of ISR[mt] are conserved from mice to men, we analyzed muscle biopsy samples of patients with MM, caused either by a single heteroplasmic mtDNA deletion or multiple mtDNA deletions, the latter caused by a dominant Twinkle mutation, homologous to that in Deletor mice (Table 1; clinical details in Spelbrink et al., 2001; Suomalainen et al., 1992, 1997). The full ISR[mt] found in Deletor mice is also activated in human patients, including *MTHFD2*, *FGF21*, *GDF15*, *PHGDH*, *PSAT1*, and *SHMT2* (mitochondrial serine hydroxymethyl-transferase-2) as well as ATF-regulated *ASNS* (asparagine synthetase) and *TRIB3* (tribbles pseudokinase 3) (Figure 1G) and UPR[mt]-linked transcription factor *DDIT3* (DNA-damage-inducible transcript 3). However, all mitochondrial HSPs or proteases remain uninduced (Figure 1G). These results indicate robust conservation of the full ISR[mt] in mammals, from mice to human patients.

ISR[mt] Progresses in Temporal Stages in Proliferating Cells after Inhibition of Mitochondrial Translation

To ask whether the temporal induction of ISR[mt] is induced in proliferating cells similar to muscle, we reversibly inhibited mitochondrial (mt)-translation in mammalian diploid myoblasts. Multiple mtDNA deletions do not accumulate in proliferating cells, inhibiting us to study exactly the same mtDNA insult in cultured cells as in Deletor muscle. However, FGF21 and GDF15 are induced in mtDNA translation diseases (Lehtonen et al., 2016), and we chose to mimic ISRmt of muscle by inhibiting mt-translation using actinonin. This drug leads to acute reversible downregulation of mt-translation and an ISR[mt]-like response (Richter et al., 2013, 2015). Figure S1 We show that ISR[mt] components are robustly induced in mouse myoblasts, following the decrease of mt-translation from the early time points (1.5–2.5 h of actinonin exposure) (Figure 2A). This response is led by >40-fold induction of *Fgf21* transcription, accompanied by *Gdf15*, *Mthfd2*, and cystathionine gamma lyase (CTH; both mRNA and protein), a regulatory enzyme of

---

Figure 1. ISR[mt] Progresses in Defined Temporal Stages in Muscle and Is Conserved in Mouse and Man

(A) Chronological progression of ISR[mt] in MM muscle. 1st stage: metabolic hormones (*Fgf21* and *Gdf15*) and mitochondrial folate cycle (Mthfd2). 2nd stage: *de novo* serine biosynthesis (*Phgdh* and *Psat1*). 3rd stage: mitochondrial HSPs. ATFs 3–5 activate at different time points. FC: mRNA against beta-actin mRNA. For details and statistical analysis, see Table S1.

(B) Progression of RC enzyme deficiency and mTORC1 activation in MM muscle. Top: histochemical *in situ* enzyme activity of COX (brown) and SDH (blue). White fibers, COX-negative; blue fibers, COX-negative, SDH positive. Bottom: phosphorylated ribosomal S6 protein (pS6 immunohistochemistry). Subsequent frozen sections; lines and arrows indicate same fibers. Scale bar, 50 μm.

(C and D) UPR[mt]-associated HSPs and proteases in skeletal muscle mitochondrial extracts; western blot. Porin and TOM20: loading controls, quantification of signals against porin in (D), n = 5 per group.

(E) Schematic representation of the temporal ISR[mt] stages of MM.

(F) ISR[mt] or UPR[mt] transcript induction in different tissues compared to beta-actin mRNA, n = 6 per group.

(G) ISR[mt] induction in human patients with MM. Tables 1 and S2 summarize subjects and details of transcript levels results, respectively.

Animal ages: 22–24 months. Bars: average and SD. Box: 25th and 75th percentiles with median and range. Dots: individual subjects. Pairwise two-tailed t test, statistical significance: *$p \leq 0.05$, **$p \leq 0.01$, ***$p \leq 0.001$, ****$p \leq 0.0001$. FC, fold change; ASNS, asparagine synthetase; ATF3–5, activating transcription factors; BAT, brown adipose tissue; CLPP, caseinolytic mitochondrial matrix peptidase; COX, cytochrome *c* oxidase; DDIT3, DNA damage inducible transcript-3; FC, fold change; FGF21, fibroblast growth factor 21; GDF15, growth and differentiation factor 15; HSP10/60/70, mitochondrial heat shock proteins 10/60/70; LONP1, lon peptidase 1; MTHFD2, methylene-tetrahydrofolate-dehydrogenase-2; mTORC1, mechanistic target of rapamycin C1; OPA1, optic atrophy 1; PHGDH, phosphoglycerate dehydrogenase; PSAT1, phosphoserine aminotransferase-1; SHMT1(2), serine hydroxymethyltransferase 1 (2, mitochondrial); SDH, succinate dehydrogenase; TOM20, translocase of outer mitochondrial membrane 20; TRIB3, tribbles pseudokinase 3; WATip/sc, white adipose tissue intraperitoneal or subcutaneous.
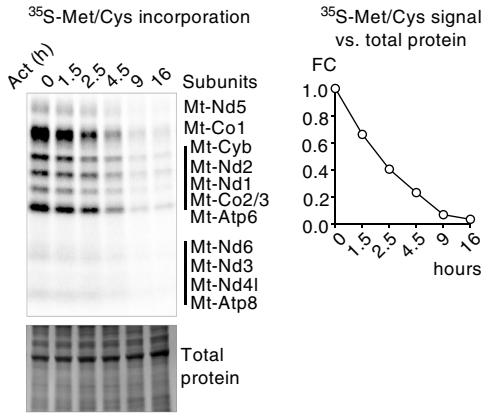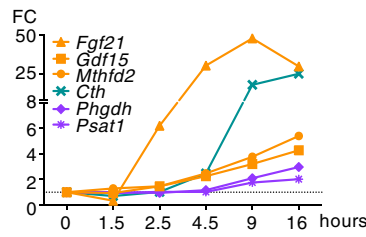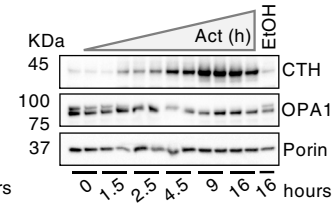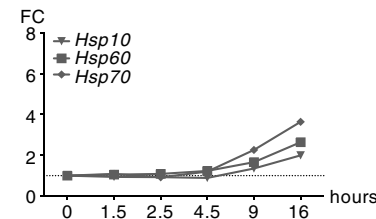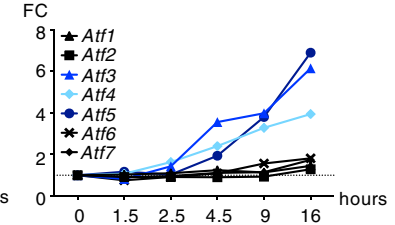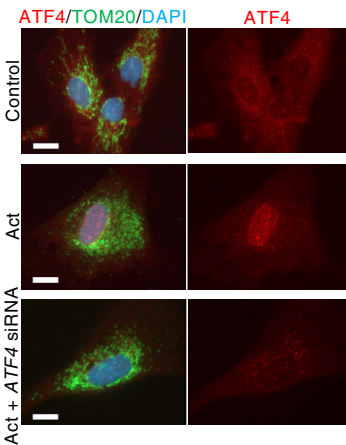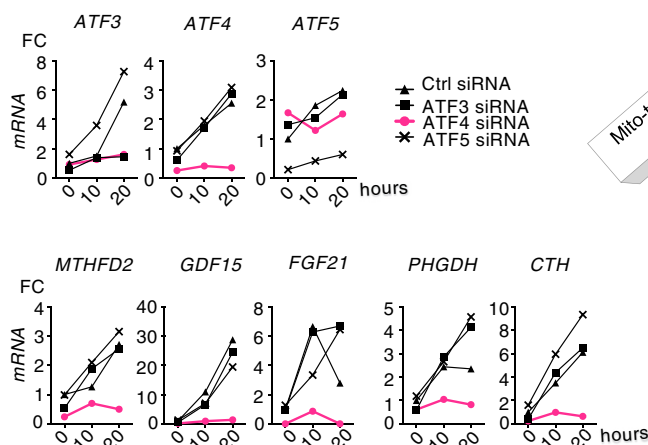
CellPress

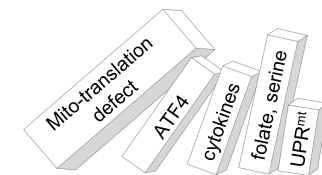**Figure 2. Temporal Progression of ISR^{mt} in Proliferating Cells after Acutely Inhibited Mitochondrial Translation**

(A) mt-translation inhibition upon actinonin exposure; ^{35}S-methionine/cysteine incorporation assay and quantification of total signal versus total protein. mt-Nd1–6, NADH dehydrogenase subunits 1–6 (complex I); mt-Cytb, cytochrome *b* (complex III); mt-Co1–3, cytochrome *c* oxidase subunits 1–3 (complex IV); mt-Atp6, mt-Atp8, ATP synthase subunits 6 and 8 (complex V).

(B) Temporal transcriptional activation of ISR^{mt} components upon mt-translation inhibition. Actinonin exposure in mouse myoblasts, mRNA quantified against beta-actin mRNA.

(C) OPA1 cleavage and progressive CTH induction upon actinonin exposure. Western blot analysis of protein extracts from mouse myoblasts, mitochondrial porin as a loading control.

(D) Temporal activation of mitochondrial HSP expression upon mt-translation inhibition; actinonin exposure, mouse myoblasts.

(E) Temporal activation of *ATF3*, *4*, and *5* expression upon mt-translation inhibition; actinonin exposure, mouse myoblasts.

(F) Nuclear localization of ATF4 upon mt-translation inhibition. Immunofluorescence analysis of untreated (top), actinonin-treated (middle), and actinonin+*ATF4* siRNA-treated (bottom) human fibroblasts; scale bar, 5 μm.

(G) ISR^{mt} induction upon mt-translation inhibition; actinonin exposure after siRNA-mediated silencing of *ATF3*, *4*, or *5* in human fibroblasts.

(H) Schematic representation of ISR^{mt} progression in growing cells, upon mt-translation inhibition.

Gene expression analyses in (B), (C), (E), and (G) represent consensus of a minimum of three separate actinonin treatment experiments. Transcripts presented in (B), (C), and (E) are measured from the same cells. Abbreviations (also see legend of Figure 1): Act, actinonin; CTH, cystathionine gamma-lyase; DAPI, 4′,6-diamidino-2-phenylindole (DNA dye); EtOH, ethanol.
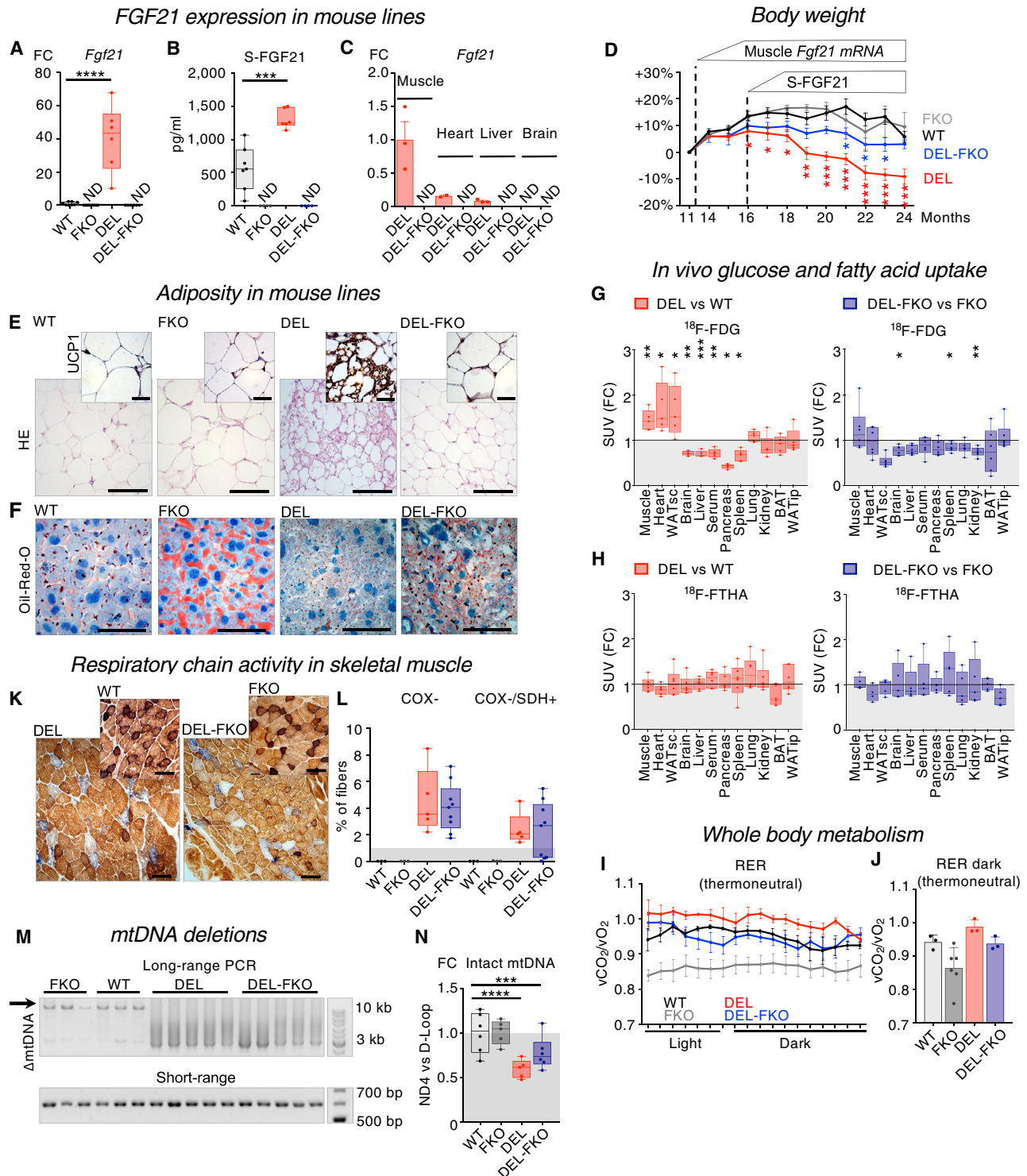
CellPress

Figure 3. Muscle-Derived FGF21 Inhibits Fat Storage and Induces Glucose Uptake without Affecting Pathological Hallmarks

(A–C) FGF21 expression in Deletor and FGF21 knockout lines; mRNA FC against beta-actin.

(A) *Fgf21* in skeletal muscle, n = 5 per group.

(B) Serum FGF21; WT, n = 7; Deletor, n = 6; FKO and DEL-FKO, n = 3.

(C) *Fgf21* expression in different tissues, compared to Deletor muscle, n = 3 per group.

(D) Body weight of mice at the age of Deletor phenotype manifestation (11–24 months). WT, FKO, n = 8; Deletor and DEL-FKO, n = 7. Significance calculated against WT mice.

(legend continued on next page)

CellPress

transsulfuration pathway (Figures 2B and 2C). Extended transla-tional stress after time point 4.5 h, the 2nd ISR^{mt} stage, upregu-lates *de novo* serine biosynthesis enzymes, together with mitochondrial HSPs (Figures 2B and 2D). These data indicate that the acute response of mammalian diploid proliferating cells to mt-translation stress is orderly and sequential, similar to the post-mitotic tissues. However, different from MM muscle, mt-translation defect ISR^{mt} involves activation of OPA1 cleavage (Figure 2C) and induction of HSPs, indicating cell-type specificity in responses to mtDNA expression defects.

ATF4 Is Required for ISR^{mt} in Dividing Cells

We then examined the contribution of the different ATFs in mouse myoblast ISR^{mt}. Out of ATFs 1–7, the expression of *ATF3*, *ATF4*, and *ATF5* gets progressively induced in mouse myoblasts upon decreasing mt-translation, whereas other *ATF*s remain uninduced (Figure 2E). Mt-translation inhibition in-creases nuclear localization of ATF4 (Figure 2F) as a sign of acti-vation of the transcription factor. To clarify the hierarchy of the ATFs, we silenced ATF3, ATF4, and ATF5 one by one. We show that ATF4 is an upstream of regulator of *CTH*, *PHGDH*, *MTHFD2*, *GDF15*, and *FGF21*, as well as *ATF3* (Figure 2G). How-ever, *ATF5* activation is independent of ATF4, which is consis-tent considering the early and progressive induction of ATF5 also in the skeletal muscle, without considerable activation of ATF4 at the time (Figure 1A). Also, mitochondrial fragmentation is not affected by ATF4 silencing (Figure 2F), suggesting its regu-lation by an ISR^{mt}-independent mechanism. ATF3 or ATF5 silencing indicates that they are not essential for ISR^{mt} induction in proliferating cells. The combined evidence from muscle and proliferating cells suggests that ATF5, ATF4, and ATF3 all take part in ISR^{mt}, with cell-type and stress specificity, fine-tuning metabolism in acute and chronic mtDNA expression stress.

FGF21 Modulates Local and Systemic Metabolism in MM

Our findings above show that FGF21 is an early responder to mtDNA replication and translation stress both in post-mitotic tis-sues and proliferating cells. To assess FGF21 contributions to disease progression and ISR^{mt}, we generated Deletor mice lack-ing FGF21. In short, Deletors with floxed *Fgf21* (FGF21$^{LoxP/LoxP}$) (Potthoff et al., 2009) were crossed with mice constitutively ex-pressing *cre*-transgene (PGK-promoter) (Lallemand et al., 1998) to generate full-body FGF21 knockout Deletors (DEL-FKO) (Figure S3A). DEL-FKO mice are unable to induce *Fgf21* expression in the affected muscle or heart or from the liver during

fasting (Figures 3A–3C and S3B), but their viability is WT-like in 24 months of follow-up.

Body weight of Deletors declines progressively from 16 to 18 months of age (Figure 3D), coinciding with the time when FGF21 becomes detectable in the blood (Figure S3C). However, *Fgf21* transcript level is high in Deletor muscle already at 12 months of age, progressively increasing from the early mani-festation of RC deficiency to ~25- to 50-fold compared to WT (Figure S3C). FGF21 knockout prevents weight loss, normalizes subcutaneous adipocyte size, and prevents WAT browning of Deletor mice (Figures 3D and 3E). Deletor liver fat is low, the small fat droplets typically residing intracellularly, whereas in WT and FKO mice, liver fat is mostly extracellular. DEL-FKO liver shows WT-like extracellular fat content, whereas FKO in healthy background leads to excessive fat accumulation (Figure 3F). These data suggest that systemic FGF21 has manifold conse-quences to liver and adipose tissue fat content in MM and ex-plains the low body weight—a symptom typical for mitochondrial disease patients.

To study the roles of FGF21 in systemic metabolism, we per-formed *in vivo* uptake assays of glucose and fatty acid analogs (^{18}F-fluorodeoxyglucose, ^{18}F-FDG; ^{18}F-Fluoro-6-thia-heptade-canoic acid, ^{18}F-FTHA). The affected muscle, heart, and brown subcutaneous WAT of Deletors shows significantly increased ^{18}F-FDG uptake (Figure 3G), normalized in DEL-FKO, indicating that FGF21 drives glucose uptake in the affected tissues in MM (Figure 3G). Fatty acid uptake (palmitic acid; saturated 16-car-bon fatty acid) is not changed in Deletor or DEL-FKO mice (Fig-ure 3H). Metabolic cage examination of systemic metabolism in Deletors (ambient temperature and thermoneutral +30°C) shows high oxygen consumption and CO_2 production, and slightly increased respiratory exchange ratio compared to WT mice, consistent with glucose usage as main fuel (Figures 3I, 3J, and S3D). In DEL-FKO mice, however, metabolism was WT-like. These results indicate that glucose is the major metabolic fuel in MM, and the disease-driven high-glucose uptake into the affected tissues is FGF21 dependent.

FGF21 Has No Effect on MM Disease Signs

The tight connection between FGF21 and advancing disease made us ask whether loss of FGF21 affected the pathologic hall-marks of MM: the RC-deficient muscle fibers, mtDNA deletions, mitochondrial mass, and RC protein amounts (Figures 3K–3N, S3E, and S3F). None of these disease signs were affected by FGF21 inactivation, demonstrating that FGF21 does not

(E) Subcutaneous adipocyte size and browning. UCP1 immunohistochemistry (scale bar, 25 μm) and H&E staining (scale bar, 100 μm).

(F) Lipid droplets in liver, Oil Red O staining for lipids and triglycerides; scale bar, 40 μm.

(G and H) *In vivo* uptake of glucose (^{18}F-FDG) and fatty acid (^{18}F-FTHA, C16:0) analogs in tissues. Statistical analysis and details in Table S3.

(I and J) Respiratory exchange ratio (RER, vCO$_2$/vO$_2$) in thermoneutral condition (+30°C). RER ~ 1, preferred fuel carbohydrates; RER ~ 0.7, lipids as fuel. Light, sleep; dark, active. (J) Average of RER when mice are active. WT, Deletor, and DEL-FKO, n = 3 per group; FKO, n = 6.

(K–N) Hallmarks of MM in skeletal muscle.

(K) Histochemical *in situ* RC enzyme activities (brown precipitate, COX-positive; white, COX-negative; blue, SDH positive, COX-negative). Scale bar, 100 μm.

(L) Quantification of (K). WT, FKO, n = 6; Deletor, n = 5; DEL-FKO, n = 8.

(M) Long-range PCR of mtDNA. Smear, multiple deletions (ΔmtDNA); arrow, full-length 16.6 kb mtDNA. Short-range PCR of mtDNA: non-deleted D-loop region (573 bp). WT and FKO, n = 3; Deletor and DEL-FKO, n = 5.

(N) qPCR analysis of full-length mtDNA (ratio of ND4 gene region and non-deleted D-loop; n = 5 per group).

Animals: 22–24 months old. Bars: average and SD. Box: 25th and 75th percentiles with median and range. Dots: individual subjects. Pairwise two-tailed t test, statistical significance: *p ≤ 0.05, **p ≤ 0.01, ***p ≤ 0.001, ****p ≤ 0.0001. Abbreviations (also see legend of Figure 1): UCP1, mitochondrial uncoupling protein 1; ^{18}F-FDG, ^{18}F-fluorodeoxyglucose; ^{18}F-FTHA, ^{18}F-fluoro-6-thia-heptadecanoic acid.

(legend on next page)

contribute to the development of mtDNA deletions, mitochondrial biogenesis, or RC deficiency in skeletal muscle.

FGF21 Regulates Serine Biosynthesis and Transsulfuration in MM

Fgf21 is a major component in the 1st stage of ISR^{mt} induction in the skeletal muscle of Deletor mice and also one of the most up-regulated transcripts in the human patient muscle. Therefore, we investigated the role of FGF21 in the progression of local muscle ISR^{mt} in MM. Intriguingly, induction of the 2nd ISR^{mt} stage is completely dependent on the presence of FGF21: *Atf3* and *Atf4*, serine *de novo* biosynthesis (*Phgdh* and *Psat1*), and transsulfuration (CTH) all are WT-like in DEL-FKO mice (Figures 4A and 4B). mTORC1 activation, however, is FGF21 independent, remaining active in RC-deficient fibers (Figure S4A). The components of the 1st ISR^{mt} stage, activated at the same time as FGF21, are unaffected by FGF21KO (*Mthfd2*, *Atf5*; ATF-regulated genes *Trib3* and *Asns*; *GDF15*) (Figures 4A and 4B). The data imply differential roles for different ATFs: *Atf3* and *Atf4* up-regulation in the 2nd ISR^{mt} stage is dependent on FGF21, whereas progressive induction of *Atf5*, starting at the 1st ISR^{mt} stage, is independently regulated in MM muscle. We also report uncoupling of regulation of mitochondrial folate cycle: MTHFD1L induction in Deletors is FGF21 dependent, whereas MTHFD2 is not (Figure 4B).

In cultured cells with mt-translation inhibition (Figure 2B), FGF21 was an early 1st ISR^{mt} responder, raising the question of whether it also regulates downstream ISR^{mt} in these cells. However, FGF21KO fibroblasts respond to actinonin similar to WT cells: both transsulfuration and *de novo* serine biosynthesis remain induced (Figure S4B). This suggests that the role of FGF21 as a regulator of ISR^{mt} progression is either stress-signal or cell-type specific. Altogether, these results show that FGF21 is essential for ISR^{mt} progression and metabolic remodeling from 1st to 2nd stage, from early to chronic, in post-mitotic skeletal muscle in MM.

As the metabolic effects of FGF21 involved biosynthetic pathways via folate-driven one-carbon cycle, we analyzed folate forms and targeted metabolome of ~100 metabolites representing the pathways of interest (Figure S4C). 5-methyl-tetrahydrofolate (THF) is rate-limiting for methyl cycle and provides one-carbon units and precursors for transsulfuration and methyl-

ation reactions. In Deletor muscle, 5-methyl-THF, betaine, choline, and glutamate required for methyl cycle and transsulfuration show high concentrations, but in DEL-FKO, their levels are WT-like (Figures 4C and S4). Figure 4D summarizes the key changes in transsulfuration between Deletors and DEL-FKO. These data suggest that (1) FGF21 drives cell-autonomous metabolic remodeling in MM, involving major biosynthetic pathways, and (2) FGF21-independent MTHFD2 (mitochondrial one-carbon cycle) does not contribute to cytoplasmic one-carbon cycle changes in MM muscle.

Amino acids show a general increase in Deletor muscle, and these levels shift to WT direction in DEL-FKO (Figure 4E). Asparagine is an exception, remaining high in DEL-FKO, consistent with increased expression of its synthesizing enzyme *Asns* in both Deletors and DEL-FKO, and suggesting glutamine usage of Deletor muscle (Zhang et al., 2014). In DEL-FKO, long-chain acylcarnitines accumulated (Figures 4F and S4C) despite the fact that their uptake was not increased (Figure 3H), suggesting inability to oxidize fatty acids in MM.

Imbalance of nucleotide metabolism intermediates and dNTPs is a metabolic hallmark of MM (Nikkanen et al., 2016), purine biosynthesis being one of the key pathways dependent on mitochondrial folate cycle (French et al., 2016). However, dNTP pools in Deletors are not improved by the absence of FGF21 (Figure 4G); actually, we show a trend toward elevated dNTPs and their precursors also in FKO, including deoxyuridine (Figure S4C). The data suggest that FGF21 has an overall inhibitory effect on dNTP homeostasis, even in normal muscle.
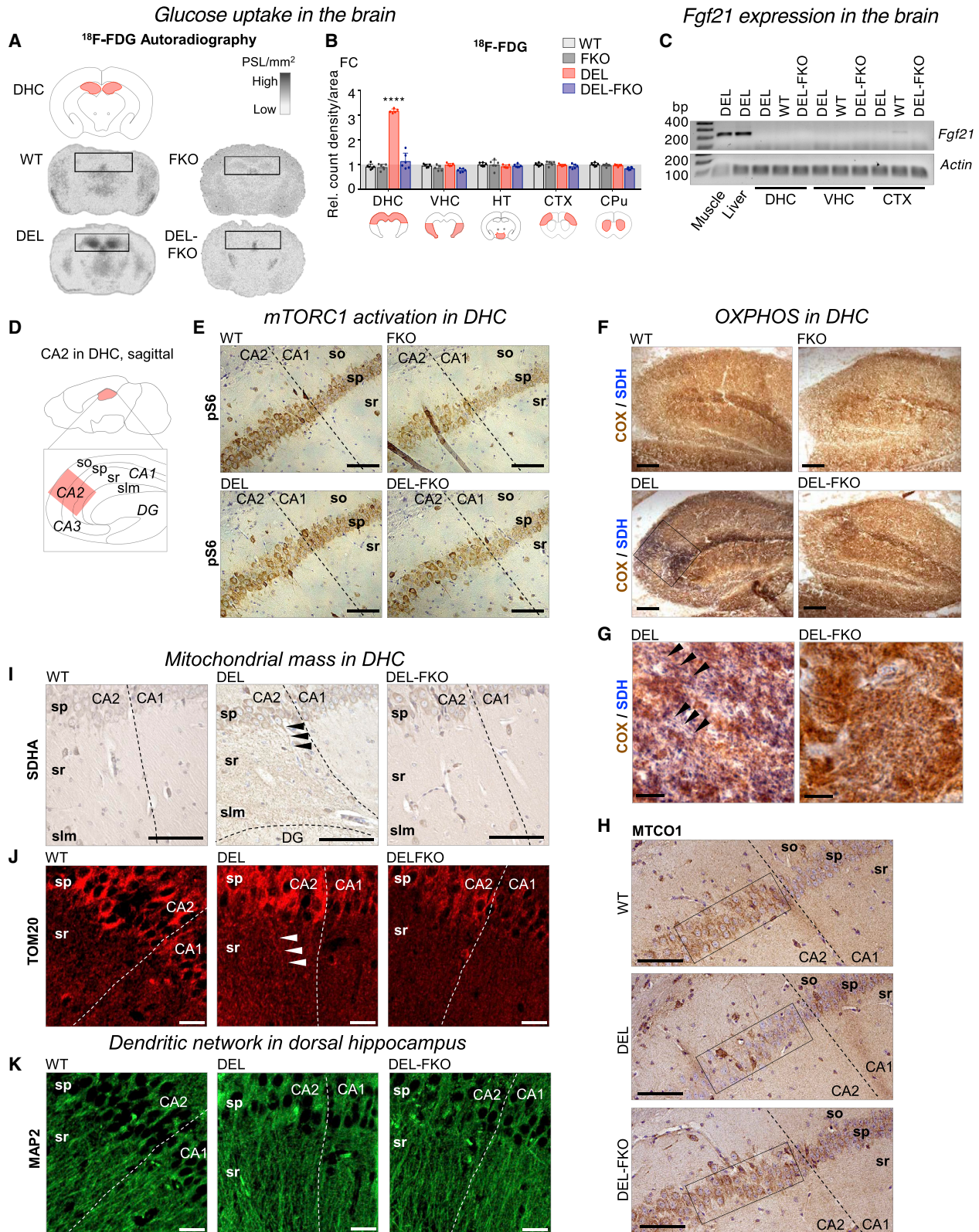
Altogether, our evidence indicates that FGF21 remodels the major anabolic biosynthesis pathways, the cytoplasmic one-carbon cycle, in MM muscle in an autocrine or paracrine manner (summarized in Figure 4H).

FGF21 Drives Glucose Uptake and Mitochondrial Proliferation in Dorsal Hippocampus in MM

FGF21 mediates signals of nutrient metabolism from peripheral organs to the brain, via binding to β-Klotho receptors in the choroid plexus and hypothalamus in WT mice (Kurosu et al., 2007; Ogawa et al., 2007; Potthoff, 2017). However, little information exists of the effects of periphery-derived FGF21 on CNS metabolism in disease. Remarkably, Deletor brain shows increased *in vivo* uptake of ^{18}F-FDG specifically in dorsal

---

Figure 4. FGF21 Regulates Induction of *De Novo* Serine Biosynthesis and Transsulfuration

(A) Differential FGF21 dependence of ATFs and ISR^{mt} expression in mouse muscle. Transcripts versus beta-actin mRNA (fold change).

(B) Differential FGF21 dependence of mitochondrial folate cycle and transsulfuration. Representative western blot analysis of protein extracts from skeletal muscle, total protein signal as loading and quantification control. n = 3/group.

(C) Dependence of methyl cycle linked metabolites on FGF21. Targeted metabolomics, significance calculated against WT. WT, FKO, n = 8; Deletor, DEL-FKO, n = 6.

(D) Schematic representation of transsulfuration pathway and linked metabolites, highlighting the FGF21-dependent changes in Deletor versus WT; DEL-FKO versus FKO. Red, increased; black, no change; gray, NA.

(E and F) Muscle amino acids and acylcarnitines. Targeted metabolomics, FC normalized to WT. Acylcarnitines shown in the order of increasing chain length (C, carnitine). Significance calculated against WT. Statistical analysis and details in Tables S4 and S5.

(G) Tissue dNTP pools, FC normalized to WT, n = 3/group.

(H) Schematic representation of folate-driven one-carbon cycle and associated biosynthetic pathways (nucleotide metabolism, methyl cycle, transsulfuration, and *de novo* serine biosynthesis) altered in Deletor. Arrows point to FGF21 effects.

Animals: 22–24 months old. Bars: average and SD. Box: 25th and 75th percentiles with median and range. Dots: individual subjects. Pairwise two-tailed t test, statistical significance: *p ≤ 0.05, **p ≤ 0.01, ***p ≤ 0.001, ****p ≤ 0.0001. Abbreviations (see also Figure 1): dNTP, deoxynucleotide; dTMP, deoxythymidine monophosphate; GCL, glutamate-cysteine ligase; Hcy, homocysteine; GS, glutathione synthetase; THF, tetrahydrofolate; SAH, S-adenosylhomocysteine; SAM, S-adenosylmethionine.

Glucose uptake in the brain

A ^{18}F-FDG Autoradiography

B ^{18}F-FDG

Fgf21 expression in the brain

C

D CA2 in DHC, sagittal

E *mTORC1 activation in DHC*

F *OXPHOS in DHC*

G

H MTCO1

I *Mitochondrial mass in DHC*

J

Dendritic network in dorsal hippocampus

K

(legend on next page)

hippocampus (DHC; CA2 region). This glucose uptake is fully FGF21 dependent (Figures 5A, 5B, and S5A). *Fgf21* transcription is not locally elevated in DHC or any region of Deletor brain (Figure 5C), suggesting that periphery-derived endocrine FGF21 mediates glucose uptake in DHC in MM. To clarify whether DHC glucose uptake reacts to FGF21 also in WT mice, we induced FGF21 expression by fasting (24 h) or by intravenous injection of recombinant FGF21, raising FGF21 serum levels 4- to 16-fold higher than in WT, respectively (Figure S5B). However, these interventions did not affect WT DHC glucose uptake (Figure S5B). These data indicate that high glucose uptake in DHC is a manifestation of MM.

Despite the lack of apparent nervous system symptoms, MM patients and Deletor mice both show mtDNA deletions in their brain (Suomalainen et al., 1992; Tyynismaa et al., 2005). DEL-FKO mice harbor similar amounts of mutant mtDNA in their DHC as the Deletors. Unlike in the muscle, however, mTORC1 activity (S6-phosphorylation) is not increased in the hippocampus of aged Deletors or DEL-FKO (Figure 5E). This conclusion is further supported by the fact that inhibition of mTORC1 activity by rapamycin does not affect *in vivo* glucose uptake in DHC (Figure S5A), indicating cell-specific roles of mTORC1 in MM.

Unlike in the Deletor muscle, mitochondrial RC activities and mitochondrial proliferation in DHC remarkably depend on presence of FGF21. SDH activity is increased in Deletor CA2 of DHC, especially in the neuronal projections spanning all the layers of CA2, while the neighboring CA1, CA3, and dentate gyrus are WT-like (Figures 5F and 5G). CA2 also shows low COX amount (Figure 5H), consistent with typical RC deficiency. Surprisingly, however, both the upregulated SDH activity and COX protein were WT-like in DEL-FKO mice, suggesting that FGF21-dependent mechanism promotes RC deficiency in CA2 of DHC (Figures 5F–5H). Immunohistological analysis of SDHA and mitochondrial outer membrane protein TOM20 confirms the increase of mitochondrial mass in CA2 neurons of Deletors and WT-like mitochondrial mass in DEL-FKO (Figures 5I and 5J). Similar appearance of pyramidal CA2 neurons and lack of astrocytosis or inflammation suggest no major neuronal damage or cell loss in Deletors or DEL-FKO (Figures 5K, S5D, and S5E). These data suggest an intriguing possibility that muscle-derived FGF21 affects RC function and mitochondrial biogenesis in the brain in MM.

DISCUSSION

Knowledge of the dynamics, regulation, and tissue-specific characteristics of mammalian stress responses in mitochondrial disease has been insufficient. Here, we report that ISR^mt is temporal and stage-wise orchestrated in mice and humans with mtDNA stress in skeletal muscle. The early ISR^mt is cell autonomous with activated expression of *FGF21*, *GDF15*, and mitochondrial one-carbon cycle, and increasing expression of *ATF5*. The 2nd disease stage activates serine and glutathione synthesis, and glucose uptake into affected tissues and systemic metabolic changes, and the 3rd terminal stage shows slight activation of *ATF3* and mitochondrial HSPs. Intriguingly, we show that progression of ISR^mt to 2nd stage is dependent on the metabolic hormone FGF21, which has major local and systemic consequences on metabolism, including in the brain. These results emphasize crosstalk of the affected and distant organ systems in mitochondrial disease and indicate that a primary mitochondrial muscle disease has major systemic consequences.

Mitochondrial stress responses have been predominantly characterized in the worm *C. elegans*, in which RNAi ablation of RC subunits induced a UPR^mt pathway as a consequence of nuclear relocation of ATFS-1, activating expression of mitochondrial HSPs and proteases (Durieux et al., 2011; Haynes et al., 2007; Nargund et al., 2012). In mammalian cancer cells, mitochondrial expression of an aggregation-prone protein elicits a UPR^mt-like response (Zhao et al., 2002), as also occurs in knockout mice for essential mitochondrial proteins (Bao et al., 2016; Ost et al., 2015; Pulliam et al., 2014; Seiferling et al., 2016). We previously described ISR^mt as the major stress response in mammalian MM. The response involved a wide transcriptional and metabolic remodeling beyond UPR^mt (Khan et al., 2017; Nikkanen et al., 2016), also found in other models with mtDNA maintenance and expression defects (*Twnk*, *Tfam*, *Polrmt*, *Lrpprc*, and *Mterf4*) (Kühl et al., 2017). Here, we show that already the first subclinical disease signs—single COX-negative muscle fibers in 10- to 12-month-old Deletor mice—activate local expression of endocrine factors FGF21 and GDF15 as well as the mitochondrial one-carbon cycle. *Fgf21* transcription is first highly upregulated in the muscle, but the

Figure 5. FGF21 Drives Glucose Uptake, Increased Mitochondrial Mass, and Respiratory Activity in CA2 of Hippocampus

(A–B) *In vivo* glucose (^{18}F-FDG) uptake in coronal brain sections; *ex vivo* digital autoradiography (ARG); photostimulated luminescence per unit area, PSL/mm².

(B) Quantification of (A), normalized to cerebellar cortex (similar cerebellar ^{18}F-FDG uptake between the groups confirmed by manual gamma ray emission measurement; data not shown). WT, FKO, DEL-FKO, n = 6; Deletor, n = 5.

(C) *Fgf21* expression in different brain areas of our mouse strains. mRNA versus beta-actin mRNA. Positive controls: deletor muscle and WT mouse liver.

(D) Schematic illustration of hippocampus and CA2 in sagittal view of mouse brain. Hippocampal layers: so, stratum oriens; sp, stratum pyramidale; sr, stratum radiatum; slm, stratum lacunosum-moleculare.

(E) Phosphorylated S6, a downstream target of mTORC1. Immunohistochemical detection at CA1/CA2 border (dotted line); scale bar, 100 μm.

(F and G) Histochemical *in situ* enzyme activity of COX (brown, active) and SDH (blue, SDH positive and COX-negative). CA2 in Deletor: increased SDH activity; scale bar, 200 μm. (G) Enlarged image of CA2 (box) of (F); arrows point to increased SDH activity in long projections (sr); scale bar, 30 μm.

(H) COX protein amount in hippocampus. Immunohistochemical detection of COX (MTCO1 antibody) in CA2 and CA1 border (dotted line). Encircled: pyramidal cell layer; Deletor, low COX-protein intensity in CA2, when compared to DEL-FKO and WT. Scale bar, 100 μm.

(I and J) Mitochondrial mass in CA2 and CA1 (border: dotted line). (I) SDH amount (SDHA antibody; increased staining in sr with dendritic extensions of pyramidal neurons). Scale bar, 100 μm. (J) Mitochondrial amount (TOM20 antibody) at CA2/CA1 border increased in extensions of pyramidal neurons (arrows, sr). Scale bar, 50 μm.

(K) Dendritic network in hippocampal CA2/CA1; MAP2 immunofluorescence. Scale bar, 50 μm.

Animals: 22–24 months old. Bars: average and SD. Dots: individual subjects. Pairwise two-tailed t test, statistical significance: *$p \leq 0.05$, **$p \leq 0.01$, ***$p \leq 0.001$, ****$p \leq 0.0001$. In histology, n = 3 per group. Abbreviations (see also Figure 1 legend): cpu, caudoputamen of striatum; CTX, cortex; DG, dentate gyrus; DHC, dorsal hippocampus; HT, hypothalamus; MAP2, microtubule-associated protein 2; VHC, ventral hippocampus; ^{18}F-FDG, ^{18}F-fluorodeoxyglucose.

protein is increased in the blood only after 4–6 months, at the same time when ragged-red fibers—a hallmark of MM—emerge in the muscle. FGF21 presence in the blood induces weight loss and WAT browning, known endocrine consequences of liver-derived FGF21 in fasting rodents (Badman et al., 2007; Xu et al., 2009). In MM muscle, the 2nd ISRmt stage activates only if FGF21 is present, with upregulated glucose uptake, *de novo* serine biogenesis, and transsulfuration. Therefore, the local and systemic 2nd ISRmt stage is crucially dependent on auto- or paracrine and endocrine effects of FGF21, which together mark the progression of the muscle disease from local to systemic. Which of the FGF21-dependent metabolic events are direct consequences of the hormone remains to be studied.

FGF21-independent components of the second ISRmt stage in the muscle include mTORC1 activation, nucleotide pool imbalance, and mitochondrial mass increase, agreeing with the previous data of mTORC1 contribution in RRF formation (Khan et al., 2017) and the regulatory role of mTORC1 for purine synthesis in cancer cells (French et al., 2016). In the hippocampus of MM mice, mitochondrial mass increase or RC deficiency is dependent on periphery-derived FGF21, but mTORC1 is not active, emphasizing tissue specificity of the responses. Overall, these data indicate that mtDNA expression defects induce an early, local subclinical response, while a second systemic, chronic stage modifies metabolism in the whole organism. These data underline the complexity of ISRmt and the essential roles of FGF21, both in the dynamics of ISRmt and progression of MM to a systemic condition.

Subtle induction of UPRmt-related mitochondrial HSPs occurs in 2-year-old Deletor mice, forming the third ISRmt stage. In mammals, this HSP response does not spread beyond the affected tissue, unlike in *C. elegans* (Durieux et al., 2011; Zhang et al., 2018). Still, the endocrine effects of muscle-derived FGF21 on hepatic lipolysis, WAT browning, brain glucose uptake, and mitochondrial mass and function mimic the "mitokine" concept of the worm: FGF21 spreads a signal of mitochondrial dysfunction from the affected organ to distant ones. The exact mechanism of how the FGF21-related muscle-to-brain signaling occurs in our mice, specifically affecting the dorsal hippocampus, requires future attention, as this region has not previously been associated with metabolic regulation or mitochondrial disease. We conclude that endocrine signaling induced by mtDNA stress, from the affected to distant tissues, is conserved from worms to mammals but in mammals is importantly contributed by FGF21, signaling from the periphery to the brain.

FGF21 had differential effects of RC deficiency and mitochondrial mass in the muscle and DHC. The dorsal hippocampus of Deletor mice showed mitochondrial mass increase and RC deficiency only in the presence of FGF21 but no changes in mtDNA deletion load. In the muscle, however, FGF21 did not affect RC activities or mitochondrial mass. mTORC1 is induced in muscle fibers with mitochondrial proliferation, but in the brain of the same animals, mTORC1 is not activated. These data underscore the remarkable tissue specificity in the upstream regulation of the mitochondrial stress responses. Importantly, our evidence indicates that a "general mitochondrial stress response" does not exist, but the specific components of ISRmt need to be characterized separately for different organisms, tissues, and insults.

ATF transcription factor family regulates the AARE response, but which homologs of the worm ATFS-1 are important in mammals has been controversial. Previously, toxin-mediated oxidative stress (paraquat) in human embryonic kidney cells was reported to induce mitochondrial HSPs in an ATF5-dependent manner (Fiorese et al., 2016). Thereafter, a multi-omics approach identified ATF4 to be the main driver of ISRmt in cervical cancer cells treated with variable inhibitors of mtDNA expression, mitochondrial protein import, or membrane potential (Quirós et al., 2017). Our data from MM mice show involvement of ATF5 and ATF3 in post-mitotic muscle, with different temporal dynamics. ATF5 expression is a robust early responder to mtDNA replication stress in both mice and human patients. In mice, ATF3 (and 4) get induced in the later stages. Interestingly, upregulation of ATF3 and ATF4 depends completely on the presence of FGF21, whereas ATF5 is FGF21 independent, further emphasizing the chronology of induction. Their roles are, however, different in proliferating cells where ATF4 gets activated early, is FGF21 independent, and is required for the activation of other ISRmt components. These data indicate that the ATF family is well conserved as a mitochondrial stress sensor from worms to mammals, but specific ATFs have different roles in different cell types and in acute or chronic stress.

In Deletors, the overall health, muscle morphology, or lifespan is not significantly affected by the presence or absence of FGF21, and they show no signs of inflammation; the major effects of FGF21 are metabolic. These findings differ from those in muscle-specific OPA1-KO mice, in which FGF21 induction was deleterious, promoting inflammation (Tezze et al., 2017), which may be explained by the difference in severity of the mitochondrial insult in OPA1-KO versus Deletor mice. Embryonic OPA1-KO in muscle is lethal at early postnatal life, and even conditional OPA1-KO in muscle results in severe muscle atrophy, rapid body weight loss, and death of the mice <100 days after induction, reflecting the vital nature of the protein (Tezze et al., 2017). Remarkably, FGF21KO in OPA1-KO animals reverted the systemic inflammation and prolonged the lifespan for >100 additional days. The results from OPA1-KO and Deletors together suggest concentration and/or context dependence of FGF21 effects, which may have clinical relevance: children with severe, often early lethal disorders of mt-translation or mtDNA maintenance have very high FGF21 concentration (up to 200-fold), whereas adults with MM show more modest induction (2- to 10-fold) (Lehtonen et al., 2016)—the former mimic FGF21 in OPA1-KO and the latter FGF21 in Deletors. These data suggest that upon severe mitochondrial dysfunction, inhibition of FGF21 might be beneficial, whereas in late-onset disorders, the mildly elevated FGF21 driving, for example, glutathione synthesis, might be protective.

Importantly, our evidence indicates that mammalian ISRmt is a complex response, with coordinated dynamics, auto/paracrine feedback loops, and endocrine signaling, affecting the whole organism, with FGF21 as its circulating messenger. The initial signal(s) that trigger the early ISRmt remain to be studied. Previous studies in cultured cells suggested the signal to involve accumulation of aberrant mt-translation products in the inner mitochondrial membrane (Richter et al., 2015). Our results highlight the systemic metabolic consequences of mitochondrial dysfunction that extend far beyond the primary RC deficiency or the affected

CellPress

organ. The usefulness of FGF21 as a therapy target remains to be studied: despite the robust morphologic and metabolic changes, the functional defects of the Deletor mice with and without FGF21 are subtle, and their lifespan normal. However, the FGF21 contribution to weight loss might be relevant for patients as well, as this is one of their most common and socially challenging symptoms. Furthermore, our results indicate that a muscle disease can affect brain metabolism, highlighting the importance of zooming out from specific tissues when considering disease pathogenesis and considering the whole organism when assessing treatment effects.

Limitations of Study

Twinkle dysfunction in the Deletor mouse and patients with MM causes progressive accumulation of mtDNA deletions in post-mitotic tissues. mtDNA deletions are typically not produced and/or maintained in replicating cell types, and the mechanistic overlap of the mitochondrial stress response in post-mitotic tissues and our cultured cell model for mt-translation stress may only be partial.

The Deletor and Deletor-FGF21KO mice have a normal lifespan and show no motor deficiency. Therefore, the effects of FGF21 or absence for the performance of the MM mice could not be tested. The evidence provided by the full-body Deletor-FGF21KO mice undisputedly shows that FGF21 is required for the metabolic phenotypes in the Deletors, especially in the muscle and brain. However, whether these phenotypes are directly FGF21 dependent, or mediated by a signaling cascade, remains to be studied.

STAR★METHODS

Detailed methods are provided in the online version of this paper and include the following:

- KEY RESOURCES TABLE
- LEAD CONTACT AND MATERIALS AVAILABILITY
  - Lead Contact
- EXPERIMENTAL MODEL AND SUBJECT DETAILS
  - Ethical Approval
  - Animal Models
  - Cell Lines
  - MEF Isolation
  - Cell Culture
  - Respiratory Function Testing in Animals
  - Tracer Assays
- METHOD DETAILS
  - Isolation of Mitochondria
  - MtDNA Deletion Load and Copy Number Determination
  - Gene Expression Analysis
  - Gene Silencing
  - Western Blotting
  - Histology
  - Quantification of FGF21
  - Metabolomics
  - dNTP Pools
  - RNA Sequencing of Patient Muscle
  - Production of Recombinant Mouse FGF21

- QUANTIFICATION AND STATISTICAL ANALYSIS
- DATA AND CODE AVAILABILITY

REFERENCES

Agnew, T., Goldsworthy, M., Aguilar, C., Morgan, A., Simon, M., Hilton, H., Esapa, C., Wu, Y., Cater, H., Bentley, L., et al. (2018). A Wars2 mutant mouse model displays OXPHOS deficiencies and activation of tissue-specific stress response pathways. Cell Rep *25*, 3315–3328.

Ahola, S., Auranen, M., Isohanni, P., Niemisalo, S., Urho, N., Buzkova, J., Velagapudi, V., Lundbom, N., Hakkarainen, A., Muurinen, T., et al. (2016). Modified Atkins diet induces subacute selective ragged-red-fiber lysis in mitochondrial myopathy patients. EMBO Mol. Med *8*, 1234–1247.

Ahola-Erkkilä, S., Carroll, C.J., Peltola-Mjösund, K., Tulkki, V., Mattila, I., Seppänen-Laakso, T., Oresic, M., Tyynismaa, H., and Suomalainen, A. (2010). Ketogenic diet slows down mitochondrial myopathy progression in mice. Hum. Mol. Genet. *19*, 1974–1984.

Badman, M.K., Pissios, P., Kennedy, A.R., Koukos, G., Flier, J.S., and Maratos-Flier, E. (2007). Hepatic fibroblast growth factor 21 is regulated by PPARalpha and is a key mediator of hepatic lipid metabolism in ketotic states. Cell Metab *5*, 426–437.

Bao, X.R., Ong, S.E., Goldberger, O., Peng, J., Sharma, R., Thompson, D.A., Vafai, S.B., Cox, A.G., Marutani, E., Ichinose, F., et al. (2016). Mitochondrial dysfunction remodels one-carbon metabolism in human cells. Elife *5*, e10575.

Dogan, S.A., Pujol, C., Maiti, P., Kukat, A., Wang, S., Hermans, S., Senft, K., Wibom, R., Rugarli, E.I., and Trifunovic, A. (2014). Tissue-specific loss of

DARS2 activates stress responses independently of respiratory chain deficiency in the heart. Cell Metab *19*, 458–469.

Durieux, J., Wolff, S., and Dillin, A. (2011). The cell-non-autonomous nature of electron transport chain-mediated longevity. Cell *144*, 79–91.

Fiorese, C.J., Schulz, A.M., Lin, Y.F., Rosin, N., Pellegrino, M.W., and Haynes, C.M. (2016). The transcription factor ATF5 mediates a mammalian mitochondrial UPR. Curr. Biol. *26*, 2037–2043.

French, J.B., Jones, S.A., Deng, H., Pedley, A.M., Kim, D., Chan, C.Y., Hu, H., Pugh, R.J., Zhao, H., Zhang, Y., et al. (2016). Spatial colocalization and functional link of purinosomes with mitochondria. Science *351*, 733–737.

Gardner, B.M., Pincus, D., Gotthardt, K., Gallagher, C.M., and Walter, P. (2013). Endoplasmic reticulum stress sensing in the unfolded protein response. Cold Spring Harb. Perspect. Biol. *5*, a013169.

Gorman, G.S., Chinnery, P.F., DiMauro, S., Hirano, M., Koga, Y., McFarland, R., Suomalainen, A., Thorburn, D.R., Zeviani, M., and Turnbull, D.M. (2016). Mitochondrial diseases. Nat. Rev. Dis. Prim *2*, 16080.

Haynes, C.M., Petrova, K., Benedetti, C., Yang, Y., and Ron, D. (2007). ClpP mediates activation of a mitochondrial unfolded protein response in C. elegans. Dev. Cell *13*, 467–480.

Haynes, C.M., Fiorese, C.J., and Lin, Y.F. (2013). Evaluating and responding to mitochondrial dysfunction: the mitochondrial unfolded-protein response and beyond. Trends Cell Biol. *23*, 311–318.

Inagaki, T., Dutchak, P., Zhao, G., Ding, X., Gautron, L., Parameswara, V., Li, Y., Goetz, R., Mohammadi, M., Esser, V., et al. (2007). Endocrine regulation of the fasting response by PPARalpha-mediated induction of fibroblast growth factor 21. Cell Metab *5*, 415–425.

Keipert, S., Ost, M., Johann, K., Imber, F., Jastroch, M., van Schothorst, E.M., Keijer, J., and Klaus, S. (2014). Skeletal muscle mitochondrial uncoupling drives endocrine cross-talk through the induction of FGF21 as a myokine. Am. J. Physiol. Endocrinol. Metab. *306*, E469–E482.

Khan, N.A., Nikkanen, J., Yatsuga, S., Jackson, C., Wang, L., Pradhan, S., Kivelä, R., Pessia, A., Velagapudi, V., and Suomalainen, A. (2017). mTORC1 regulates mitochondrial integrated stress response and mitochondrial myopathy progression. Cell Metab.26 *26*, 419–428.e5.

Kharitonenkov, A., and Shanafelt, A.B. (2009). FGF21: a novel prospect for the treatment of metabolic diseases. Curr. Opin. Investig. Drugs *10*, 359–364.

Kharitonenkov, A., Shiyanova, T.L., Koester, A., Ford, A.M., Micanovic, R., Galbreath, E.J., Sandusky, G.E., Hammond, L.J., Moyers, J.S., Owens, R.A., et al. (2005). FGF-21 as a novel metabolic regulator. J. Clin. Invest *115*, 1627–1635.

Kühl, I., Miranda, M., Atanassov, I., Kuznetsova, I., Hinze, Y., Mourier, A., Filipovska, A., and Larsson, N.G. (2017). Transcriptomic and proteomic landscape of mitochondrial dysfunction reveals secondary coenzyme Q deficiency in mammals. Elife *6*, e30952.

Kurosu, H., Choi, M., Ogawa, Y., Dickson, A.S., Goetz, R., Eliseenkova, A.V., Mohammadi, M., Rosenblatt, K.P., Kliewer, S.A., and Kuro-o, M. (2007). Tissue-specific expression of betaKlotho and fibroblast growth factor (FGF) receptor isoforms determines metabolic activity of FGF19 and FGF21. J. Biol. Chem. *282*, 26687–26695.

Lallemand, Y., Luria, V., Haffner-Krausz, R., and Lonai, P. (1998). Maternally expressed PGK-Cre transgene as a tool for early and uniform activation of the Cre site-specific recombinase. Transgenic Res. *7*, 105–112.

Lehtonen, J.M., Forsström, S., Bottani, E., Viscomi, C., Baris, O.R., Isoniemi, H., Höckerstedt, K., Österlund, P., Hurme, M., Jylhävä, J., et al. (2016). FGF21 is a biomarker for mitochondrial translation and mtDNA maintenance disorders. Neurology *87*, 2290–2299.

MacVicar, T., and Langer, T. (2016). OPA1 processing in cell death and disease - the long and short of it. J. Cell Sci. *129*, 2297–2306.

Martí, R., Dorado, B., and Hirano, M. (2012). Measurement of mitochondrial dNTP pools. Methods Mol. Biol. *837*, 135–148.

Merkwirth, C., Jovaisaite, V., Durieux, J., Matilainen, O., Jordan, S.D., Quiros, P.M., Steffen, K.K., Williams, E.G., Mouchiroud, L., Tronnes, S.U., et al. (2016). Two conserved histone demethylases regulate mitochondrial stress-induced longevity. Cell *165*, 1209–1223.

Nandania, J., Kokkonen, M., Euro, L., and Velagapudi, V. (2018a). Simultaneous measurement of folate cycle intermediates in different biological matrices using liquid chromatography-tandem mass spectrometry. J. Chromatogr. B Analyt. Technol. Biomed. Life Sci. *1092*, 168–178.

Nandania, J., Peddinti, G., Pessia, A., Kokkonen, M., and Velagapudi, V. (2018b). Validation and automation of a high-throughput multitargeted method for semiquantification of endogenous metabolites from different biological matrices using tandem mass spectrometry. Metabolites *8*.

Nargund, A.M., Pellegrino, M.W., Fiorese, C.J., Baker, B.M., and Haynes, C.M. (2012). Mitochondrial import efficiency of ATFS-1 regulates mitochondrial UPR activation. Science *337*, 587–590.

Nikkanen, J., Forsström, S., Euro, L., Paetau, I., Kohnz, R.A., Wang, L., Chilov, D., Viinamäki, J., Roivainen, A., Marjamäki, P., et al. (2016). Mitochondrial DNA replication defects disturb cellular dNTP pools and remodel one-carbon metabolism. Cell Metab *23*, 635–648.

Nunnari, J., and Suomalainen, A. (2012). Mitochondria: in sickness and in health. Cell *148*, 1145–1159.

Ogawa, Y., Kurosu, H., Yamamoto, M., Nandi, A., Rosenblatt, K.P., Goetz, R., Eliseenkova, A.V., Mohammadi, M., and Kuro-o, M. (2007). BetaKlotho is required for metabolic activity of fibroblast growth factor 21. Proc. Natl. Acad. Sci. USA *104*, 7432–7437.

Olichon, A., Baricault, L., Gas, N., Guillou, E., Valette, A., Belenguer, P., and Lenaers, G. (2003). Loss of OPA1 perturbates the mitochondrial inner membrane structure and integrity, leading to cytochrome c release and apoptosis. J. Biol. Chem. *278*, 7743–7746.

Ost, M., Keipert, S., van Schothorst, E.M., Donner, V., van der Stelt, I., Kipp, A.P., Petzke, K.J., Jove, M., Pamplona, R., Portero-Otin, M., et al. (2015). Muscle mitohormesis promotes cellular survival via serine/glycine pathway flux. FASEB J *29*, 1314–1328.

Ost, M., Coleman, V., Voigt, A., van Schothorst, E.M., Keipert, S., van der Stelt, I., Ringel, S., Graja, A., Ambrosi, T., Kipp, A.P., et al. (2016). Muscle mitochondrial stress adaptation operates independently of endogenous FGF21 action. Mol. Metab *5*, 79–90.

Pereira, R.O., Tadinada, S.M., Zasadny, F.M., Oliveira, K.J., Pires, K.M.P., Olvera, A., Jeffers, J., Souvenir, R., McGlauflin, R., Seei, A., et al. (2017). OPA1 deficiency promotes secretion of FGF21 from muscle that prevents obesity and insulin resistance. EMBO J *36*, 2126–2145.

Potthoff, M.J. (2017). FGF21 and metabolic disease in 2016: a new frontier in FGF21 biology. Nat. Rev. Endocrinol *13*, 74–76.

Potthoff, M.J., Inagaki, T., Satapati, S., Ding, X., He, T., Goetz, R., Mohammadi, M., Finck, B.N., Mangelsdorf, D.J., Kliewer, S.A., et al. (2009). FGF21 induces PGC-1alpha and regulates carbohydrate and fatty acid metabolism during the adaptive starvation response. Proc. Natl. Acad. Sci. USA *106*, 10853–10858.

Pulliam, D.A., Deepa, S.S., Liu, Y., Hill, S., Lin, A.L., Bhattacharya, A., Shi, Y., Sloane, L., Viscomi, C., Zeviani, M., et al. (2014). Complex IV-deficient Surf1(-/-) mice initiate mitochondrial stress responses. Biochem. J. *462*, 359–371.

Quirós, P.M., Prado, M.A., Zamboni, N., D'Amico, D., Williams, R.W., Finley, D., Gygi, S.P., and Auwerx, J. (2017). Multi-omics analysis identifies ATF4 as a key regulator of the mitochondrial stress response in mammals. J. Cell Biol. *216*, 2027–2045.

Richter, U., Lahtinen, T., Marttinen, P., Myöhänen, M., Greco, D., Cannino, G., Jacobs, H.T., Lietzén, N., Nyman, T.A., and Battersby, B.J. (2013). A mitochondrial ribosomal and RNA decay pathway blocks cell proliferation. Curr. Biol. *23*, 535–541.

Richter, U., Lahtinen, T., Marttinen, P., Suomi, F., and Battersby, B.J. (2015). Quality control of mitochondrial protein synthesis is required for membrane integrity and cell fitness. J. Cell Biol. *211*, 373–389.

Richter, U., Ng, K.Y., Suomi, F., Marttinen, P., Turunen, T., Jackson, C., Suomalainen, A., Vihinen, H., Jokitalo, E., Nyman, T.A., et al. (2019). Mitochondrial stress response triggered by defects in protein synthesis quality control. Life Sci. Alliance *2*.

CellPress

Rygiel, K.A., Grady, J.P., Taylor, R.W., Tuppen, H.A.L., and Turnbull, D.M. (2015). Triplex real-time PCR - an improved method to detect a wide spectrum of mitochondrial DNA deletions in single cells. Sci. Rep 5, 9906.

Seiferling, D., Szczepanowska, K., Becker, C., Senft, K., Hermans, S., Maiti, P., König, T., Kukat, A., and Trifunovic, A. (2016). Loss of CLPP alleviates mitochondrial cardiomyopathy without affecting the mammalian UPRmt. EMBO Rep 17, 953–964.

Sidrauski, C., and Walter, P. (1997). The transmembrane kinase Ire1p is a site-specific endonuclease that initiates mRNA splicing in the unfolded protein response. Cell 90, 1031–1039.

Spelbrink, J.N., Li, F.Y., Tiranti, V., Nikali, K., Yuan, Q.P., Tariq, M., Wanrooij, S., Garrido, N., Comi, G., Morandi, L., et al. (2001). Human mitochondrial DNA deletions associated with mutations in the gene encoding Twinkle, a phage T7 gene 4-like protein localized in mitochondria. Nat. Genet. 28, 223–231.

Suomalainen, A., and Battersby, B.J. (2018). Mitochondrial diseases: the contribution of organelle stress responses to pathology. Nat. Rev. Mol. Cell Biol. 19, 77–92.

Suomalainen, A., Majander, A., Haltia, M., Somer, H., Lönnqvist, J., Savontaus, M.L., and Peltonen, L. (1992). Multiple deletions of mitochondrial DNA in several tissues of a patient with severe retarded depression and familial progressive external ophthalmoplegia. J. Clin. Invest 90, 61–66.

Suomalainen, A., Majander, A., Wallin, M., Setälä, K., Kontula, K., Leinonen, H., Salmi, T., Paetau, A., Haltia, M., Valanne, L., et al. (1997). Autosomal dominant progressive external ophthalmoplegia with multiple deletions of mtDNA: clinical, biochemical, and molecular genetic features of the 10q-linked disease. Neurology 48, 1244–1253.

Suomalainen, A., Elo, J.M., Pietiläinen, K.H., Hakonen, A.H., Sevastianova, K., Korpela, M., Isohanni, P., Marjavaara, S.K., Tyni, T., Kiuru-Enari, S., et al. (2011). FGF-21 as a biomarker for muscle-manifesting mitochondrial respiratory chain deficiencies: a diagnostic study. Lancet Neurol. 10, 806–818.

Taylor, R.C., and Dillin, A. (2013). XBP-1 is a cell-nonautonomous regulator of stress resistance and longevity. Cell 153, 1435–1447.

Tezze, C., Romanello, V., Desbats, M.A., Fadini, G.P., Albiero, M., Favaro, G., Ciciliot, S., Soriano, M.E., Morbidoni, V., Cerqua, C., et al. (2017). Age-associated loss of OPA1 in muscle impacts muscle mass, metabolic homeostasis, systemic inflammation, and epithelial senescence. Cell Metab. 25, 1374–1389.

Tyynismaa, H., Mjosund, K.P., Wanrooij, S., Lappalainen, I., Ylikallio, E., Jalanko, A., Spelbrink, J.N., Paetau, A., and Suomalainen, A. (2005). Mutant mitochondrial helicase Twinkle causes multiple mtDNA deletions and a late-onset mitochondrial disease in mice. Proc. Natl. Acad. Sci. USA 102, 17687–17692.

Tyynismaa, H., Carroll, C.J., Raimundo, N., Ahola-Erkkilä, S., Wenz, T., Ruhanen, H., Guse, K., Hemminki, A., Peltola-Mjøsund, K.E., Tulkki, V., et al. (2010). Mitochondrial myopathy induces a starvation-like response. Hum. Mol. Genet. 19, 3948–3958.

Xu, J., Lloyd, D.J., Hale, C., Stanislaus, S., Chen, M., Sivits, G., Vonderfecht, S., Hecht, R., Li, Y.S., Lindberg, R.A., et al. (2009). Fibroblast growth factor 21 reverses hepatic steatosis, increases energy expenditure, and improves insulin sensitivity in diet-induced obese mice. Diabetes 58, 250–259.

Zhang, Z., Tsukikawa, M., Peng, M., Polyak, E., Nakamaru-Ogiso, E., Ostrovsky, J., McCormack, S., Place, E., Clarke, C., Reiner, G., et al. (2013). Primary respiratory chain disease causes tissue-specific dysregulation of the global transcriptome and nutrient-sensing signaling network. PLoS One 8, e69282.

Zhang, J., Fan, J., Venneti, S., Cross, J.R., Takagi, T., Bhinder, B., Djaballah, H., Kanai, M., Cheng, E.H., Judkins, A.R., et al. (2014). Asparagine plays a critical role in regulating cellular adaptation to glutamine depletion. Mol. Cell 56, 205–218.

Zhang, Q., Wu, X., Chen, P., Liu, L., Xin, N., Tian, Y., and Dillin, A. (2018). The mitochondrial unfolded protein response is mediated cell-non-autonomously by Retromer-dependent Wnt signaling. Cell 174, 870–883.

Zhao, Q., Wang, J., Levichkin, I.V., Stasinopoulos, S., Ryan, M.T., and Hoogenraad, N.J. (2002). A mitochondrial specific stress response in mammalian cells. EMBO J. 21, 4411–4419.

CellPress

STAR★METHODS

KEY RESOURCES TABLE

REAGENT or RESOURCE	SOURCE	IDENTIFIER
Antibodies		
Mouse-anti-ATF4	Santa Cruz	Cat# sc-390063; RRID:AB_2810998
Goat-anti-β-ACTIN	Santa Cruz	Cat# sc-1616; RRID:AB_630836
Rabbit anti-BiP	Cell Signaling	Cat# 3177; RRID:AB_2119845
Rabbit anti-CLPP	Proteintech	Cat# 15698-1-AP; RRID:AB_2245115
Rabbit anti-CTH/CSE	Proteintech	Cat# 12217-1-AP; RRID:AB_2087497
Rabbit anti-HSP10	Abcam	Cat# ab108600; RRID:AB_10864371
Rabbit anti-HSP60	Abcam	Cat# ab46798; RRID:AB_881444
Rabbit anti-HSP70	Abcam	Cat# ab53098; RRID:AB_880311
Rabbit anti-LONP1	Sigma	Cat# HPA002192; RRID:AB_1079695
Rabbit anti-MTHFD2	Abcam	Cat# ab37840, RRID:AB_776544
Rabbit anti-MTHFD1L	Proteintech	Cat# 16113-1-AP, RRID:AB_2250974
Rabbit anti-OPA1	BD Biosciences	Cat# 612606; RRID:AB_399888
Rabbit anti-PORIN	Abcam	Cat# ab15895; RRID:AB_2214787
Mouse anti-SDHA	Abcam	Cat# ab14715; RRID:AB_301433
Rabbit anti-TOM20	Santa Cruz	Cat# sc-11415; RRID:AB_2207533
Rabbit anti-Vinculin	Abcam	Cat# ab129002; RRID:AB_11144129
Rabbit anti-UCP1	Abcam	Cat# ab10983; RRID:AB_2241462
Rabbit anti-phospho-S6	Cell Signaling Technology	Cat# 4858; RRID:AB_916156
Rabbit anti-GFAP	Millipore	Cat# AB5804; RRID:AB_2109645
Rabbit anti-IBA1	Wako	Cat# 019-19741; RRID:AB_839504
Chicken anti-MAP2	Abcam	Cat# ab5392; RRID:AB_2138153
Goat anti-mouse IgG	Jackson ImmunoResearch	Cat# 115-035-146; RRID:AB_2307392
Goat anti-rabbit IgG	Jackson ImmunoResearch	Cat# 111-035-144; RRID:AB_2307391
Rabbit anti-goat IgG	Millipore	Cat# 401504-2ML; RRID:AB_437813
Goat anti-rabbit IgG Alexa Fluor®488	Abcam	Cat# ab150077
Goat anti-chicken IgG Alexa Fluor®405	Abcam	Cat# ab175674
Donkey anti-rabbit IgG Alexa Fluor®594	Abcam	Cat# ab150068
Bacterial and Virus Strains		
BL21(DE3) *E. coli* cells (with pET-SUMO-FGF21)	Suomalainen Lab	N/A
Chemicals, Peptides, and Recombinant Proteins		
^{18}F-FTHA (^{18}F-Fluoro-6-thia-heptadecanoic acid)	Suomalainen Lab	N/A
^{18}F-FDG (^{18}F-Fludeoxyglucose)	Suomalainen Lab	N/A
Recombinant FGF21	Suomalainen Lab	N/A
Rapamycin	LC Laboratories	Cat#R-5000
DMSO	Sigma Aldrich	Cat#D8418
PEG-400	Sigma Aldrich	Cat#202398
Phosphatase inhibitor cocktail	Thermo Scientific	Cat#78420
SYBR Green Supermix	Bio-Rad	Cat#1725006CUST
Protein assay kit	Bio-Rad	Cat#500-0114
Pierce Protease Inhibitor Mini Tablets, EDTA-Free	Thermo Scientific	Cat#88666
Actinonin	Sigma Aldrich	Cat#A6671
JET Prime transfection reagent	Polypus	Cat#114-07
Uridine	Calbiochem	Cat#6680
Dexamethasone	Sigma Aldrich	Cat#D1756

CellPress

Continued

REAGENT or RESOURCE	SOURCE	IDENTIFIER
Insulin	Sigma Aldrich	Cat#I-1882
Fetuin	Sigma Aldrich	Cat#F-2379
Phusion High-Fidelity DNA Polymerase	Thermo Scientific	Cat#530L
Oil Red O	Sigma Aldrich	Cat#O0625
Glutaraldehyde solution	Sigma Aldrich	Cat#G7651
TRIzol Reagent	Thermo Scientific	Cat#15596026
RNeasy Mini Kit	Qiagen	Cat# 74104
Formic Acid	VWR CHEMICALS	Cat#84865.290
Citric Acid	Sigma Aldrich	Cat#251275
Acetonitrile	VWR CHEMICALS	Cat#1.59014.2500
Phenylmethylsulfonyl fluoride	Sigma Aldrich	Cat# 10837091001
3, 3 –diaminobenzidine (DAB)	Sigma Aldrich	Cat#D8001
Cytochrome c	Sigma Aldrich	Cat#C2506
Sodium succinate	Sigma Aldrich	Cat#S2378
Catalase	Sigma Aldrich	Cat#C9322
Nitro Blue Tetrazolium	Sigma Aldrich	Cat#N5514
MitoTracker™ Red CMXRos	Thermo Scientific	Cat# M7512
VECTASTAIN Elite ABC-Peroxidase Kit	Vector Laboratories	Cat# PK-6101; RRID:AB_2336820
Antibody Diluent, Background Reducing	Agilent, Dako	Cat# S3022
VECTASHIELD® Antifade Mounting Medium with DAPI	Vector Laboratories	Cat# H-1200
Champion™ pET SUMO Expression System	Thermo Scientific	Cat# K30001
HisTrap FF Crude, 5	GE Healthcare	Cat# 11000458
HisTrap FF 1ml	GE Healthcare	Cat# 17531901
HiTrap Desalting columns with Sephadex G-25 resin	GE Healthcare	Cat# 17140801
HiTrap DEAE Sepharose FF	GE Healthcare	Cat# 17515401
Superdex 75 10/300 GL	Ge healthcare	Cat# 17517401
SUMO protease	Thermo Scientific	Cat# 12588018
Bio-Beads SM-2 resin	Bio-Rad	Cat# 1523920
Critical Commercial Assays		
Mouse/Rat FGF-21 Quantikine ELISA Kit	R&D Systems	Cat#MF2100
Maxima First Strand cDNA Synthesis Kit for RT-qPCR	Thermo Scientific	Cat#K1671
Deposited Data		
Human muscle biopsy RNA-Seq data	Gene Expression Omnibus data repository	GEO: GSE129811
Experimental Models: Cell Lines		
Mouse myoblasts C2C12	ATCC	CRL-1772
Human diploid myoblast male control line (established in-lab)	Suomalainen Lab	#2572
Human diploid fibroblasts male control line (established in-lab)	This study	#3532
Experimental Models: Organisms / Strains		
Tg/ACTB/twnk-p.353-365-dup/BL6	Suomalainen Lab	N/A
Fgf21LoxP/LoxP	Steven A. Kliewer	(Potthoff et al., 2009)
Tg(Pgk1-cre)1Lni	The Jackson Laboratory	B6.C-Tg(Pgk1-cre)1Lni/CrsJ, Stock No:020811
Oligonucleotides		
See Table S6 for primer sequences	This paper	N/A
siRNA Control 1/2	ThermoFisher	Cat#s4390843/46
siRNA ATF3	ThermoFisher	Cat# s1699/s1701
siRNA ATF4	ThermoFisher	Cat# s1703/04
siRNA ATF5	ThermoFisher	Cat# s22424/25

(Continued on next page)

CellPress

Continued

REAGENT or RESOURCE	SOURCE	IDENTIFIER
Software and Algorithms		
AIDA image analysis software	Elysia Raytest	N/A
Fiji / ImageJ software	NIH	N/A
STAR 2.5.0a	GenSoft	N/A
HTSeq 0.10.0	Simon Anders	N/A
DESeq2 1.18.1 package	Bioconductor	N/A
Prism v.7	GraphPad Software	N/A
Other		
Mouse diet	Altromin Spezialfutter	Cat#C1000

LEAD CONTACT AND MATERIALS AVAILABILITY

Lead Contact
Requests and detailed information of reagents should be directed to and will be made available by the Lead Contact, Anu Suomalainen (anu.wartiovaara@helsinki.fi).

EXPERIMENTAL MODEL AND SUBJECT DETAILS

Ethical Approval
The National Animal Experiment Review Board and Regional State Administrative Agency for Southern Finland approved the animal experimentation, following the European Union Directive. The human materials were collected and used with informed consent according to the Helsinki Declaration and approved by the Ethical Review Board of Helsinki University Central Hospital.

Animal Models
The Deletor mice expressed a dominant in-frame duplication, homologous to a human mitochondrial myopathy mutation. Two previously reported transgene lines were used in this study. We generated the Deletor mouse with Fgf21 knockout by utilizing the Cre-Lox recombination system (Figure S3A). The heterozygous Twinkle$^{dup\ 353-365}$ (Deletor) males and PGK-Cre females were first crossed for two generations with Fgf21$^{LoxP/LoxP}$. The Deletor x Fgf21$^{LoxP/LoxP}$ males were then crossed with PGK-Cre x Fgf21$^{LoxP/LoxP}$ females. PGK-Cre has ubiquitous expression. All genotypes were born in the expected Mendelian ratios and were viable. An equal percentage of animals (80-86%) in all study groups survived until euthanizing at 22-24 months of age. The population was maintained with crosses between Deletor-FKO males and FKO females. Male mice were used for all analyses because of slightly more pronounced findings of mitochondrial myopathy in Deletor males than females.

Cell Lines
The human fibroblasts cell line was established from a healthy 45-years-old male Caucasian donor via skin biopsy using routine protocols. Primary low passaged human myoblasts were from a healthy voluntary 45-years-old male Caucasian donor (Ahola et al., 2016). Murine C2C12 myoblasts were obtained from ATCC.

MEF Isolation
Embryonic fibroblasts were cultured from E13.5 WT and FGF21KO mouse embryos. Embryos were collected in phosphate-buffered saline (1xPBS, without calcium and magnesium ions) and the head and liver were separated. Remaining tissue material was cut into small pieces and homogenized in 5% trypsin in 1xPBS (1ml/embryo). This suspension was incubated at +37°C and mixed by pipetting every 5 minutes. 1ml of this suspension was added to 9 ml of DMEM media supplemented with GlutaMax (Gibco), 10% FBS, amino acids (MEM Non-Essential Amino Acids Solution, Thermo Fisher) and penicillin/streptomycin. Cells were plated on gelatin-coated dishes. Confluent dishes were split the following day and harvested on day 3-4 by trypsinization for further analyses.

Cell Culture
Human myoblasts from a healthy 45-year-old male Caucasian donor (Khan et al., 2017) were grown in 420 ml Ham's F10 with GlutaMax (Gibco 41550-021) supplemented with 75 ml of heat-inactivated fetal bovine serum (FBS, Sigma, F9665), 250 mg bovine serum albumin (BSA, Sigma #A-4503), 250 mg fetuin (Sigma #F-2379), 90 mg insulin (Sigma #I-1882), 5 ml of 39 μg/ml dexamethasone (Sigma, #D1756), 500 μl epidermal growth factor (10 μg/ml, BD Biosciences, 354052), 10 mg uridine (Calbiochem, 6680). All other cells were grown in Dulbecco's Modified Eagle's Medium DMEM (Sigma-Aldrich), with 4.5 g/l glucose supplemented with 10% fetal bovine serum, 20 mM pyruvate, 100 units/ml of penicillin/streptomycin and 50 μM uridine. All cells were maintained in a humidified chamber at 37°C at 5% CO_2.

CellPress

Respiratory Function Testing in Animals

Oxygen consumption and carbon dioxide production were measured in Oxymax Lab Animal Monitoring System (CLAMS; Columbus Instruments). In CLAMS the mice were housed in individual cages in temperature-regulated chamber, settled for 24 hours and were recorded for 2 days. The settling and the first day of recording were in room temperature (+22°C) followed by 24 hours at thermo-neutral conditions (+30°C). Respiratory exchange ratio (RER) was calculated to indicate a rough estimate of the preferred fuel (carbohydrate breakdown vs. fatty acid oxidation) of the organism.

Tracer Assays

Pre-conditioning

For fasting experiments food was removed after initial feeding period at 7-9 pm (beginning of dark period) and tracer uptake took place in the following morning after 24 hours of fasting.

For FGF21 injection experiments, animals were intraperitoneally injected 4 hours prior to tracer injection with either saline placebo or recombinant mouse FGF21 (see details for production in method details). The injected dose for recombinant FGF21 was 0.06 mg/kg.

Rapamycin treatment was made according to Khan et al. (2017). Rapamycin (LC Laboratories #R-5000) was dissolved in DMSO to yield stock of 100 mg/ml, further diluted in 5% PEG-400 to final concentration of 1.2 mg/ml. Solution was sterile filtered and stored at −80°C prior to use. Before administration, the mice were weighed and the dose was adjusted to 8 mg/kg/day. Mice were injected intraperitoneally for 6 weeks.

Assay Protocol

Prior to all tracer uptake assays, food was removed from cages for 3 hours. The animals were kept in anesthesia with small dose of inhaled isoflurane (1-1,5% in oxygen or room air carrier) on temperature-controlled mats throughout the procedure. Glucose analog ^{18}F-FDG (^{18}F-Fludeoxyglucose; total activity injected 5MBq) or fatty acid analog ^{18}F-FTHA (^{18}F-Fluoro-6-thia-heptadecanoic acid; total activity 5MBq) was administered intravenously. The uptake periods for ^{18}F-FDG and ^{18}F-FTHA were 60 and 30 minutes, respectively. Biodistribution of tracers was assayed by detecting gamma rays emitted from excised tissues with manual gamma counter. Standardized uptake values (SUV) in different tissues were calculated for each sample. Quantitative phosphor imaging autoradiography of ^{18}F-FDG in brain was performed after 60 minutes of *in vivo* uptake period. Coronal brain cryosections (20 μm) were cut on objective glass and exposed on imaging plate (plate (Fuji BAS-TR2025) for approximately 3.5 hours. The plates were scanned with Fuji BAS-5000 Phosphor imager with 25 μm resolution (digital autoradiography, ARG). The ARG images were analyzed for count densities (photostimulated luminescence per unit area, PSL/mm^2) with a computerized image analysis program (AIDA image analyzer). Cerebellar cortex was selected to be the reference brain region for signal normalization as it showed equal uptake in all study groups in *ex vivo* tissue-panel assay.

METHOD DETAILS

Isolation of Mitochondria

Mitochondria were isolated from quadriceps femoris (QF) from Deletors to enrich for mitochondrial protein. QF was homogenized in a Potter-Elvejhem with a rotor-driven pestle in HIM buffer (10 mM HEPES-KOH, pH7.6, 100 mM KCl, 3 mM MgCl2, 0.1 mM EDTA, 10% glycerol, 0.1% fatty-acid free BSA) supplemented with 1 mM PMSF and protease inhibitors (Sigma). One QF was lysed in 5 ml HIM buffer, strained with a 100 μm cell strainer and sieve rewashed with 5 ml homogenization buffer. Enriched mitochondrial fractions were obtained by differential centrifugation at a low step at 700xg for 20 min and resulting supernatant at 10'000xg for 10 min and was repeated. All steps were performed at 4°C.

MtDNA Deletion Load and Copy Number Determination

Total cellular DNA was isolated from frozen quadriceps femoris (QF) by standard proteinase K and phenol–chloroform method. For determination mtDNA deletion load we used long-range PCR reactions for deleted and undeleted fractions of mtDNA (Ahola-Erkkila et al., 2010) using primers in non-deleted region between 16S rRNA and ND1 to enable partly deleted mtDNA molecules. 10 ng of total genomic DNA was amplified with primers for long template PCR using Phusion high-fidelity DNA polymerase (Thermo Fisher) and supplied GC buffer PCR reaction was initial denaturation for 30 s at 98°C, 22 cycles of 10 s at 98°C and 12 min extension at 72°C and a final extension step for 10 min at 72°C. For total mtDNA amount determination a non-deleted mtDNA fragment was amplified using Phusion high fidelity DNA polymerase and GC buffer: initial denaturation of 30 s at 98°C; 21 cycles of 10 s at 98°C and 2 min at 72°C; final extension step of 10 min at 72°C. All PCR products were agarose gel (1%) electrophoresed and imaged using ChemiDoc™ XRS+ System (Bio-Rad). Amount of the total mtDNA product was compared to the deleted mtDNA products.

Alternatively, mtDNA deletion load was determined by a modified a triplex assay (Rygiel et al., 2015) adapted for mice. The mouse triplex assay was used for single-well detection using 5'-modified primers with ROX (D-Loop probe), HEX (ND1 probe) or FAM (ND4 probe) for single-well detection. Primer efficiency and linear range of amplification was determined by serial dilution. A standard curve was included in every run. All primer sequences can be found from Table S6.

Gene Expression Analysis

RNA was extracted by standard Trizol-chloroform precipitation for tissues and by using the Qiagen miRNA kit for cells. DNase digestion was performed and total RNA reverse transcribed using the Maxima first strand RT (ThermoFisher). 10-20 mg of tissue were used for homogenization. Total cellular RNA was extracted from snap frozen tissues in TRIzol reagent (Invitrogen) and homogenized with Fast-Prep w-24 Lysing Matrix D (MP Biomedical) and Precellys w-24 (Bertin Technologies). RNA of cultured cells was directly lysed in TRIzol and extracted. RNA concentration was measured with NanoDrop1000 Spectrophotometer and integrity checked in agarose gel electrophoresis. Two micrograms of RNA was DNAse treated (Ambion). One microgram of total RNA was used to generate cDNA using Maxima first-strand cDNA synthesis kit (Thermo Scientific). Quantitative real-time PCR amplification of cDNA was performed with IQ SybrGreen kit (Bio-Rad) on CFX96 Touch qPCR system (Bio-Rad). Relative expressions were normalized to β-actin or 18S rRNA as indicated. All primer sequences can be found from Table S6.

Gene Silencing

Gene silencing was performed using SilencerSelect (ThermoFisher) siRNAs for control siRNA 1 (s4390843) & 2 (s4390846) and against ATF4 (s1703, s1704), ATF3 (s1699, s1701), ATF5 (s22424, s22425). Briefly, two consecutive rounds of 25 picomoles of siRNAs per 6 cm^2 dish were used to transfect human fibroblasts on day 1 at 50% confluency and day 4 in order to achieve maximum knockdown efficiency using Polyplus jetPRIME transfection kit. Transfection efficiency was confirmed by RT-qPCR.

Western Blotting

Total protein from cells was extracted using RIPA buffer supplemented with phosphatase inhibitors (ThermoFisher Scientific) and sodium orthovanadate in order to preserve phosphorylation sites. Briefly, tissues (20 mg) were homogenized in 20-30 volumes of 1XTBS with bead homogenizer (5000 beats for 20s) (Precellys) and Triton-X was added to yield 1% volume of the extract. The mixture was incubated on ice for 30 min and collected by centrifugation at 14,000xg for 20 min. Protein concentrations were determined using Bradford assay. Proteins were separated in appropriate gels by SDS-PAGE usually on 4-20% gradient gels, transferred to polyvinylidene difluoride (PVDF) membranes and blocked with 5% milk or 3% BSA in 1xTBS-T (Tris Buffered Saline with 0.1% Tween20) for 1 h and primary antibodies incubated overnight at 4°C, Ab concentration range according to manufacturer's instructions (1:250-1:1000) in 3% BSA in TBS-T buffer. Antibodies used are listed in key resources table. Secondary HRP antibodies were used in 1:10000 dilution in 5% milk in TBS-T and signal detected by Clarity Western ECL Substrate (Biorad) with ChemiDoc™ XRS+ System (Biorad). Signal intensities were quantified by ImageLab 5.2.1 (Biorad).

Histology

Respiratory Chain Enzyme Activity and Oil-red-O, Fresh-frozen Tissues

Tissues were freshly embedded in OCT medium (Tissue-Tek) and frozen in 2-methylbutane bath under liquid nitrogen cooling.

Simultaneous histochemical activity analysis of cytochrome-c-oxidase (COX) and succinate dehydrogenase (SDH) activities was performed on QF and brain slices (12 μm), incubation times being 30 minutes for COX (RT) and 40 minutes for SDH (+37°C). Buffer contents for COX: 0.05 M phosphate buffer (pH 7.4) with 3, 3 –diaminobenzidine (DAB), catalase, cytochrome c and sucrose and for SDH: 0.05 M phosphate buffer (pH 7.4) with nitro-blue tetrazolium and sodium succinate. After stainings the slices were dehydrated in ascending alcohols, xylene-treated and mounted. From muscle sections, COX-negative/SDH-negative, COX-negative/SDH-positive and normal fibers were quantified.

For Oil-Red-O staining 8 μm sections of frozen liver were fixed in formic calcium and incubated in Oil-Red-O solution for 10 min followed by brief hematoxylin staining for nuclei.

Immunohistochemistry in Tissues

Tissues were fixed in 10% buffered formalin and embedded in paraffin. Citric acid antigen retrieval and H$_2$O$_2$ treatment were performed. The samples were blocked for non-specific staining by incubating for 30 min in 2% horse serum. Primary antibody incubations were performed overnight at 4°C. Detection was done with Vectastain Elite ABC HRP Kit according to the manufacturer's instructions followed by chromogen DAB staining. The nuclei were briefly counterstained with hematoxylin. Antibodies: SDHA (Complex II) Abcam, ab14715 (1:500); UCP1 Abcam, ab10983 (1:500).

Immunofluorescence in Tissues

Tissues were fixed in 10% buffered formalin and embedded in paraffin. Citric acid antigen retrieval was performed. The samples were blocked for non-specific staining by incubating for 30 min in 2% horse serum. Incubation with antibodies was done in Antibody diluent (Dako), primary antibody incubation for overnight at 4°C and secondary in room temperature with appropriate Alexa Fluor® antibodies (from Abcam). Antibodies: GFAP from Millipore, AB5804 (1:500); IBA1 from Wako, 019-19741 (1:1000); MAP2 from Abcam, ab5392 (1:500) and TOM20 from Santa Cruz, sc-11415 (1:500).

Adipocytes

Formalin-fixed paraffin-embedded sections were stained with hematoxylin and eosin.

Staining in Cells

Living cells grown on cover slips were stained for 15 min in 50 nM Mitotracker CMXRos in full media, rinsed with 1xPBS and fixed in ice-cold acetone or directly fixed in ice-cold acetone for immunofluorescence stainings. Fixed samples were blocked (5% horse serum, 1% BSA, 0.1% Triton-X-100 in 1xPBS) and incubated with the primary antibodies against TOM20 (SantaCruz, #11415, 1:250) and ATF4 (SantaCruz B-3, sc390063) overnight. Secondary anti-rabbit Alexa488 was used for TOM20 and anti-mouse

CellPress

Alexa594 for ATF4. All samples were mounted in VectaShield (Vector Laboratories) containing DAPI to counterstain for nuclei. Images were recorded on a Zeiss AxioImager 1.2 equipped with an ApoTome.

Electron Microscopy

Attached cells were directly fixed in 2% glutaraldehyde in phosphate buffer, post-fixed in 1% osmium tetroxide and dehydrated through ascending concentrations of alcohol and embedded in Epon812. 60nm ultrathin sections were obtained on a Reichert-Jung Ultracut ultramicrotome equipped with Diatome (Switzerland) diamond knife, transferred to copper grids, stained with uranyl acetate and lead citrate and observed in a Philips CM12 electron microscope at 80kV. Images were recorded with a Morada digital camera and analyzed using iTEM software.

Quantification of FGF21

Terminal blood samples were collected via heart puncture, were let to coagulate for 15 minutes at room temperature and centrifuged at 4°C at 3,000x g for 15 minutes. Separated serum was frozen and stored in -80°C prior to assay. Mouse/Rat FGF21 Qusntikine ELISA (R&D Systems) was used according to manufacturer's instructions. Absorbance measurement was made with SpectraMax 190 absorbance microtiter plate reader.

Metabolomics

Metabolomic analyses were performed from 20 mg of muscle extract using Waters Acquity ultra performance liquid chromatography (UPLC) and triple-quadrupole mass spectrometry analysis in FIMM (Institute for Molecular Medicine Finland). All metabolite standards, ammonium formate, ammonium acetate and ammonium hydroxide were obtained from Sigma-Aldrich (Helsinki, Finland). Formic acid (FA), 2-proponol, acetonitrile (ACN), and methanol (all HiPerSolv CHROMANORM, HPLC grade, BDH prolabo) were purchased from VWR International (Helsinki, Finland). Isotopically labelled internal standards were purchased from Cambridge Isotope Laboratory. The exact procedure is described and validated in Nandania et al. (2018a), (2018b). The polar metabolome was extracted from frozen 20 mg mouse muscle and lysed with a Precellys homogenizer in 1.4 mm ceramic (Zirconium oxide) beads containing tubes including 10 µl of labeled internal standard mix and 1:20 sample: extraction solvent in a two-step extraction protocol. The first step contained 10 parts of 100% ACN + 1% FA for 3 cycles at 5500 rpm with 30s pausing in-between. Sample was centrifuged at -20°C at 2 min in an Eppendorf 5404R centrifuge at 5000 rpm and supernatant collected. The remaining pellet was re-lysed with 10 parts of 80/20%ACN/H_2O + 1% FA as described above. Calibration solutions were serially diluted in a 96-well plate. Samples were analyzed on an ACQUITY UPLC-MS/MS system (Waters Corporation, Milford, MA, USA) with specific settings reported in Nandania et al. (2018b). Detection was performed on a Xevo TQ-S tandem triple quadrupole mass spectrometer (Waters, Milford, MA, USA), was operated in both positive and negative polarity. Samples were ionized by electro spray ionization (ESI) and dwell time and subsequent data acquisition were automatically calculated by MassLynx 4.1 software and processed using TargetLynx software. Quantification was performed by internal standards and external calibration curves.

dNTP Pools

Total dNTP pool measurements were performed and analyzed as described (Martí et al., 2012; Nikkanen et al., 2016). Approximately 50-100 mg of frozen muscle tissue was homogenized in 10 volumes (v/w) homogenization buffer (10 mM Tris/HCl, pH 7.5, 0.2 mM ethylene glycol tetra-acetic acid (EGTA), 0.5 % bovine serum albumin (BSA), 210 mM mannitol, 70 mM sucrose) using a polytron homogenizer. Obtained homogenate was centrifuged for 10 min at 4°C. Cold methanol (-20°C) was added to the resulting supernatants for a final concentration of 60% (v/v) and stored at -80°C for 3h. Samples were then heated to 95°C for 3 min, cooled on ice and centrifuged at 16000 x g at 4°C for 20 min. Obtained supernatants were collected and dried down. Appropriate amounts of re-hydrated extracts were added to the reaction mix containing 40 mM Tris/HCl, pH 7.5, 10 mM $MgCl_2$, 5 mM dithiothreitol (DTT) and 0.25 µm specific primed oligonucleotide, 0.75 µm ^{3}H-dTTP or ^{3}H-dATP, 0.30-unit Taq DNA polymerase for a total of 20 µl and incubated for 60 min at 48°C. 15 µl of reaction mix was spotted onto DE-81 filter paper and dried. Spotted samples were then washed 3x with 5% Na_2HPO_4, 1x water and 1x with 95% ethanol. Reaction products were analyzed using a liquid scintillation counter with 3-6 measurements per individual sample and quantified compared to standard curves.

RNA Sequencing of Patient Muscle

A Bergström needle biopsy from *vastus lateralis* was collected from eight controls and from four PEO patients. Total muscle RNA was extracted with standard TRIzol and chloroform method and purified with RNA purification kit (RNeasy; Qiagen). A total of one microgram of total RNA was used for global transcriptomics analysis performed by the Beijing Genomic Institute (BGI) using their standard protocols. In brief, transcriptome sequencing was performed using 50bp paired-end sequencing on an Illumina sequencing platform. The resulting raw reads were preprocessed by the sequencing provider to filter out reads failing criteria for quality, unknown base and adaptor sequence content. Clean reads, specified in FASTQ format, amounted to approximately 26 million reads per sample. Subsequent analysis was performed in-house and reads were aligned against the GRCh38 Human genome assembly (DNA primary assembly in FASTA format and gene annotation in GTF format from Ensembl release 92) using STAR 2.5.0a, giving read alignments in BAM format. Counting of reads mapping to genes was performed with htseq-count, HTSeq 0.10.0, in union overlap resolution mode. The obtained read counts were then used for differential gene expression analysis with the Bioconductor DESeq2 1.18.1 package. Fold changes in binary logarithmic scale and respective p-values were extracted for pairwise comparisons.

CellPress

Production of Recombinant Mouse FGF21

Cloning and Expression

Champion pET SUMO Protein Expression system was used. BL21(DE3) *E. coli* cells with pET-SUMO-FGF21 expression vector were grown at +32°C in Luria-Bertani media until the OD600 was 0.6-0.8. Then, 0.3 mM of isopropyl-D-thiogalactoside (IPTG) was added to induce expression of the fusion protein and cells were grown for another 4 hours. Cell cultures were pelleted at 8000 rpm for 10 min at +4°C, washed with 25mM Tris-HCl, pH7.5, 200mM NaCl, centrifuged for 15 min at 5000rpm, +4°C and frozen at -20°C.

Purification

Whole purification procedure was performed at +4°C. All chromatography steps were done on AktaPurifier 10 (GE Healthcare). A cell pellet harvested from 1 L of culture was melted, suspended in 50ml of 20mM NaH_2PO_4, pH7.6, 150 mM NaCl, 0.5mM PMSF and disrupted by sonication. Cell lysate was ultra-centrifuged at 40,000 rpm for 30 min and supernatant was collected. NaCl and imidazole were added to yield final concentrations of 500 mM and 20mM, respectively. Protein solution was filtered through 0.45μm PVDF filter (Millipore) and loaded at 3 ml/min flow rate onto HisTrap Crude FF 5ml column (GE Healthcare) equilibrated with 20mM NaH_2PO_4, pH 7.6, 500 mM NaCl containing 20 mM imidazole. After washing with 10 x column volume of 20 mM imidazole and 5 x column volume of 50 mM imidazole, the his-tagged sumo-FGF21 fusion was eluted with 200 mM imidazole in the equilibration buffer. Eluate was concentrated with 10 kDa cut-off Vivaspin concentrators (Millipore), protein was desalted against 20mM NaH_2PO_4, pH 7.6 using HiTrap Desalting column 5ml (GE Healthcare) at 3 ml/min flow rate. Then the protein was loaded at 3ml/min flow rate onto HiTrap DEAE FF 5ml column (GE Healthcare), equilibrated with 20mM NaH_2PO_4, pH 7.6. After washing with 120mM NaCl, the protein was eluted with 200 mM NaCl in the equilibration buffer. Pooled fractions with eluted protein were concentrated to 1ml in Vivaspin concentrators with 10kDa cut-off (Millipore) and desalted on HiTrap Desalting column 5ml (GE Healthcare) against 5 mM TrisHCl, pH 8.0, 155 mM NaCl. Cleavage of sumo tag was performed using SUMO protease (Thermo Scientific) according to manufacturer's instructions. After removal of NP-40 with BioBeads (Bio-Rad) followed by adjustment of NaCl concentration to 500mM and imidazole concentration to 20 mM the protein solution was loaded at 0.5 ml/min onto HisTrap FF 1 ml column (GE Healthcare) equilibrated with 20mM NaH_2PO_4, pH 7.6, 500 mM NaCl, 20 mM imidazole. Flow through containing FGF21 was concentrated to 400μl in Vivaspin concentrators and loaded onto Superdex 75 10/300 GL column equilibrated with PBS, pH7.4. Gel filtration was run at 0.2 ml/min. Fractions containing FGF21 were pooled and concentrated. Protein concentration was determined using Bradford method with bovine serum albumin as a standard.

QUANTIFICATION AND STATISTICAL ANALYSIS

Statistical analyses and their graphical representation were performed in GraphPad Prism v.7.0 software (GraphPad Software, USA). Statistical test used in each experiment is indicated in figure legend. P-values of less than 0.05 were considered statistically significant. Outlier analysis for all analyses was done using GraphPad Prism 7.0 ROUT method (Q=1%) and false positive analysis for metabolomics with Benjamin-Hochberg method, critical value of 0.2.

DATA AND CODE AVAILABILITY

All data generated or analyzed during this study are included in this published article and its supplementary information files. Materials used in this study are available from the corresponding author on reasonable request. Human muscle biopsy RNA-Seq data deposited to Gene Expression Omnibus data repository with accession number GEO: GSE129811.